iScience

CellPress
OPEN ACCESS

Article

Vitamin C-reduced graphene oxide improves the performance and stability of multimodal neural microelectrodes

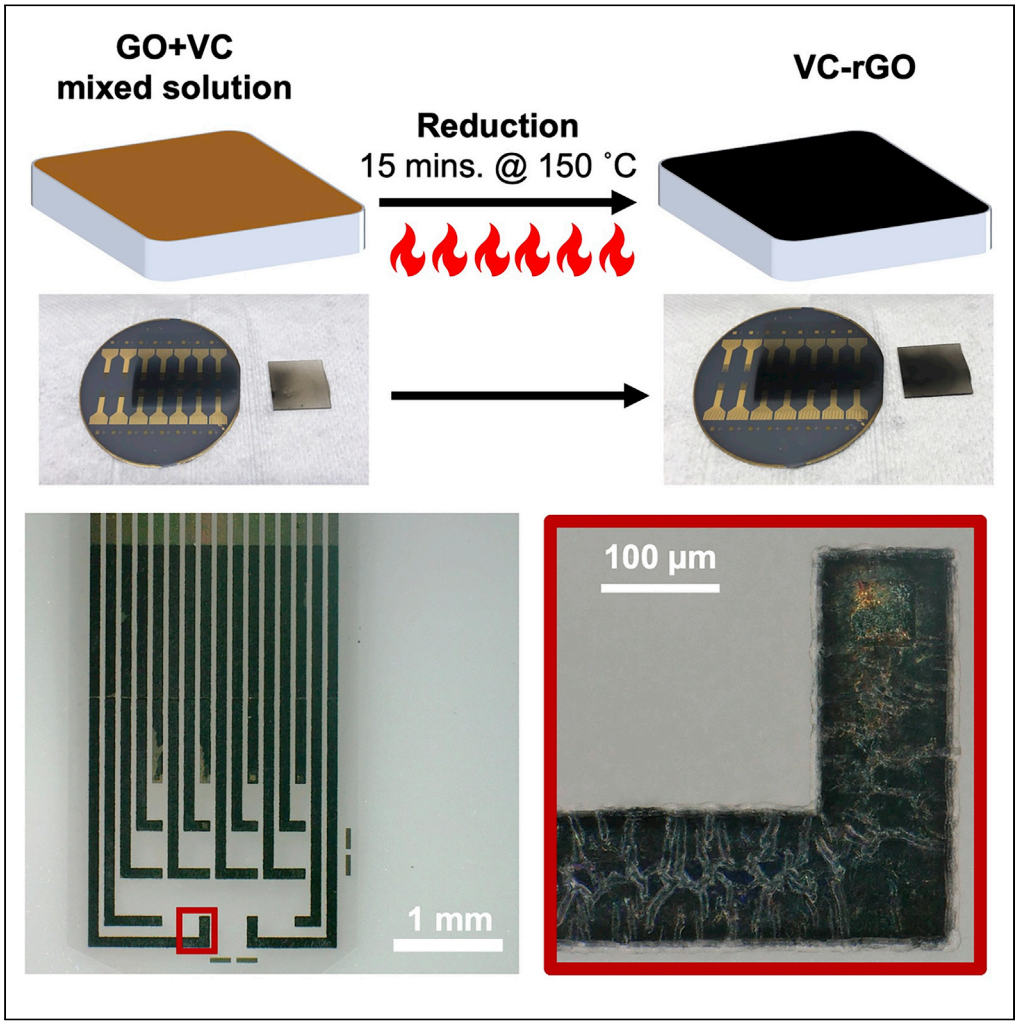

Brendan B. Murphy, Nicholas V. Apollo, Placid Unegbu, ..., Francesca Cimino, Andrew G. Richardson, Flavia Vitale

vitalef@pennmedicine.upenn.edu

Highlights

Easy, scalable, and safe reduction method to create rGO films with vitamin C

VC-rGO coatings improve the performance of bare gold microelectrodes *in vitro*

VC-rGO coatings enable the voltammetric detection of dopamine on the microscale

rGO/Au electrode arrays enable high-resolution microscale recording *in vivo*

Murphy et al., iScience *25*, 104652
July 15, 2022
https://doi.org/10.1016/j.isci.2022.104652

iScience

CellPress
OPEN ACCESS

Article

Vitamin C-reduced graphene oxide improves the performance and stability of multimodal neural microelectrodes

Brendan B. Murphy,[1,2,3,9] Nicholas V. Apollo,[1,2,3,8,9] Placid Unegbu,[1,2,3] Tessa Posey,[4] Nancy Rodriguez-Perez,[5] Quincy Hendricks,[1,2] Francesca Cimino,[1,2] Andrew G. Richardson,[2,6] and Flavia Vitale[1,2,3,7,10,*]

SUMMARY

Nanocarbons are often employed as coatings for neural electrodes to enhance surface area. However, processing and integrating them into microfabrication flows requires complex and harmful chemical and heating conditions. This article presents a safe, scalable, cost-effective method to produce reduced graphene oxide (rGO) coatings using vitamin C (VC) as the reducing agent. We spray coat GO + VC mixtures onto target substrates, and then heat samples for 15 min at 150°C. The resulting rGO films have conductivities of ~44 S cm^{-1}, and are easily integrated into an *ad hoc* microfabrication flow. The rGO/Au microelectrodes show ~8x lower impedance and ~400x higher capacitance than bare Au, resulting in significantly enhanced charge storage and injection capacity. We subsequently use rGO/Au arrays to detect dopamine *in vitro*, and to map cortical activity intraoperatively over rat whisker barrel cortex, demonstrating that conductive VC-rGO coatings improve the performance and stability of multimodal microelectrodes for different applications.

INTRODUCTION

Our understanding of the circuitry underlying brain function and disease is largely informed by the ability to record and modulate neural activity with high-fidelity electrodes. Typically, these are composed of inorganic materials such as doped silicon (Si), platinum (Pt), gold (Au), and iridium oxide (IrOx), as they are adequately conductive and biocompatible, electrochemically stable, and easy to pattern into a variety of structures using standard lithographic techniques. However, resolving the spatial (10–100 μm) and temporal (1–10 ms) scales governing cellular-level activity requires miniaturizing the electrode contacts (Kellis et al., 2016). Microscale electrodes based on these materials typically exhibit high impedance (>1 MΩ) and modest charge injection capacities, which degrade the signal-to-noise ratio (SNR) of recordings and limit safe neuromodulation (Cogan, 2008; Ludwig et al., 2011; Boehler et al., 2020). Furthermore, monitoring the dynamics of biochemical species is crucial to investigate mechanisms of neural function and disease, but electrodes with limited surface area and appropriate surface chemistry suffer from low sensitivities and sub-optimal detection limits above physiological levels (Roychaudhuri, 2015).

Common strategies to overcome these limitations are nanoscale roughening and coatings on the surface of metallic or Si electrodes (Aregueta-Robles et al., 2014), which result in a higher effective surface area and additional adsorption sites for analytic detection (Cogan, 2008). The overall effect is an increase in the electrochemical double-layer capacitance, leading to impedance reduction and enhanced capacity to store and safely deliver stimulation charge. Common materials used for electrode surface enhancements include: titanium nitride (TiN) (Zhang et al., 2017; Khan et al., 2019), nanoscale carbons like carbon nanotubes (CNTs) (Keefer et al., 2008; Shoval et al., 2009) and nanodiamonds (Turcheniuk and Mochalin, 2017; Puthongkham and Venton, 2019), conductive polymers (CPs) such as polypyrrole (PPy) (Harris et al., 2013) and poly(3,4-ethylenedioxythiophene) doped with polystyrene sulphonate (PEDOT:PSS) (Ludwig et al., 2011; Castagnola et al., 2015; Ganji et al., 2017a; Ganji et al., 2017b; Aqrawe et al., 2019), and hybrids of these materials (Behler et al., 2009; Castagnola et al., 2009; Luo et al., 2011; Sriprachuabwong et al., 2012; Kolarcik et al., 2014; Zhang et al., 2017). However, TiN is an extremely stiff ceramic that requires high-temperature processing and specialized nitridation treatments to be effective (Zhang et al., 2017; Feng et al., 2019). Nanocarbon coatings also require complex chemical modifications to promote adhesion

[1]Department of Bioengineering, University of Pennsylvania, Philadelphia, PA 19104, USA

[2]Center for Neuroengineering and Therapeutics, University of Pennsylvania, Philadelphia, PA 19104, USA

[3]Center for Neurotrauma, Neurodegeneration and Restoration, Corporal Michael J. Crescenz Veterans Affairs Medical Center, Philadelphia, PA 19104, USA

[4]Department of Biomedical Engineering, University of South Carolina, Columbia, SC 29206, USA

[5]School of Sustainable Engineering and the Built Environment, Arizona State University, Tempe, AZ 85281, USA

[6]Department of Neurosurgery, University of Pennsylvania, Philadelphia, PA 19104, USA

[7]Department of Physical Medicine and Rehabilitation, University of Pennsylvania, Philadelphia, PA 19146, USA

[8]Present address: Advanced Bionics LLC, 28515 Westinghouse Place, Valencia, CA 91355, USA

[9]These authors contributed equally

[10]Lead contact

*Correspondence: vitalef@pennmedicine.upenn.edu

https://doi.org/10.1016/j.isci.2022.104652

to most electrode surfaces (Keefer et al., 2008; Kostarelos, Bianco and Prato, 2009; Aregueta-Robles et al., 2014). Similarly, CPs are often electrochemically polymerized onto the target substrate, followed by additional post-processing to selectively coat only the exposed contact sites (Harris et al., 2013; Aregueta-Robles et al., 2014; Castagnola et al., 2015). Even if directly cast as thin films onto the target substrate—as is possible with solution-processable materials, such as PEDOT:PSS (Khodagholy et al., 2015; Ganji et al., 2017a; Ganji et al., 2017b)—many CP coatings still suffer from degradation, mechanical failure, and delamination, due to multiple factors including poor adhesion (Green et al., 2012) and excessive thickness of the coating layer (Cui and Zhou, 2007).

Reduced graphene oxide (rGO) is an attractive coating material for neural electrodes due to its predominantly capacitive nature, electrochemical stability, ease of processing and tunability, and lower impedance and higher charge delivery characteristics compared to metals and Si (Apollo et al., 2015; Wang et al., 2019; Hejazi et al., 2020a, 2020b). In the context of electrode technologies, rGO, like many other hybrid carbon-based nanomaterials (Laurila et al., 2017), has been primarily explored as a surface area enhancing material for biochemical sensors (Robinson et al., 2008; Wang et al., 2009; Shao et al., 2010; Wang et al., 2014; Yang et al., 2014; Ng et al., 2015; Fang et al., 2017), while only a few works have used rGO for neural recording and stimulation (Apollo et al., 2015; Liu et al., 2015b; Dalrymple et al., 2019; Wang et al., 2019). For most biosensing applications, rGO films have been produced by direct reduction of dry films of its hydrophilic precursor, graphene oxide (GO) (Alazmi et al., 2016). Many of these post-assembly reduction steps typically involve exposure to hydrazine vapor (Gilje et al., 2007; Stankovich et al., 2007; Becerril et al., 2008; Eda et al., 2008; Wallace et al., 2008) or high temperature annealing at temperatures $T > 1{,}000°C$ (Chen et al., 2016; Wang et al., 2018). However, these processes pose serious health and safety concerns (Zhang et al., 2010; Ding et al., 2015), and may also be incompatible with other electrode components, such as encapsulating polymers. For materials such as parylene-C, polyimide (PI), SU-8, and polyethylene terephthalate (PET), the glass transition temperature (T_g) lies in the ~120°C–300°C range (Yokota et al., 2001; Harder et al., 2002; Lin et al., 2011; Chung and Park, 2013; Kahouli et al., 2014), which precludes high temperature annealing. Furthermore, it has been shown that hydrazine causes long-term degradation of a variety of polymeric films (Dine-Hart et al., 1971; Goel et al., 2009).

Alternative reduction methods consist of liquid-phase reduction via strong acids, such as hydrochloric (Ning et al., 2014) and hydriodic (Lin et al., 2013) acids, or ammonia-rich mixtures (Wallace et al., 2008; Pham et al., 2010). In these processes, GO and the reducing agent are mixed at moderate temperatures ($T > 60°C$) for a few minutes, followed by vacuum filtration to form the rGO films (Wallace et al., 2008; Fernandez-Merino et al., 2010). However, rGO solutions suffer from colloidal instability (Xu et al., 2014; Liu et al., 2015a) and surfactants like *N*-methyl-2-pyrrolidone (NMP) or dimethylformamide (DMF) are typically required (Park and Ruoff, 2009). Both NMP and DMF are cytotoxic (Salavagione et al., 2017), and although Cyrene might be a more biocompatible alternative, its long-term stability and safety have not been fully characterized (Salavagione et al., 2017; Pan et al., 2018). Furthermore, surfactants typically lower the electronic conductivity of the final rGO films (Fernández-Merino et al., 2012). Recently, *L*-ascorbic acid—a.k.a. vitamin C (VC)—has been established as a viable, biocompatible, and safe GO reducing agent (Dua et al., 2010; Zhang et al., 2010; Fernandez-Merino et al., 2010; Ding et al., 2015). In previous studies, VC-mediated GO reduction was conducted in solution, and rGO films were subsequently processed from the reduced suspensions by vacuum filtration. However, vacuum filtration results in large-area films (typically 90–120 μm in thickness), which are difficult to handle, transfer, and pattern, and which are prone to damage during subsequent manufacturing steps. Thus, vacuum filtration is largely incompatible with standard microfabrication processes, and would particularly hinder scale-up of the process to reliably and repeatably fabricate neural electrodes. An alternative, high-through, solutions-based method would therefore be more desirable for realizing rGO-based coatings for neural technologies, as this could be easily integrated into standard fabrication flows for microelectrodes.

In the present work, we propose a novel method to produce rGO coatings for neural microelectrode arrays that is safe, high-throughput, compatible with common electrode materials, and easy to integrate into standard microelectrode fabrication processes. Taking advantage of the slow reaction kinetics of VC as a reducing agent at room temperature (Zhang et al., 2010; Fernandez-Merino et al., 2010; Abulizi et al., 2014), we demonstrate the direct fabrication of rGO-coated neural microelectrode arrays, using GO + VC mixtures spray cast onto bare Au contacts micropatterned on Si wafers. To maximize the electronic and electrochemical properties of the coatings, we have optimized processing parameters such as VC

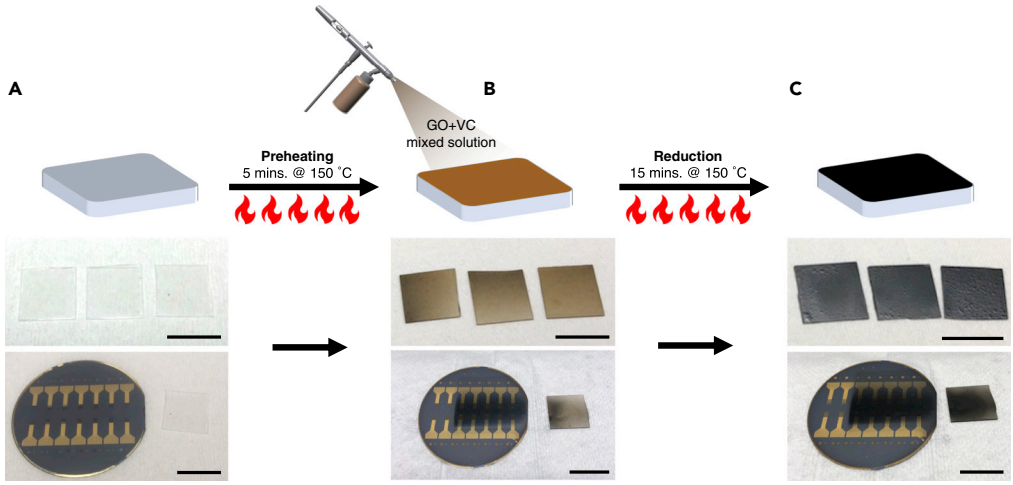

Figure 1. VC-rGO thin film fabrication flow

(A) The substrate is preheated to 150°C for 5 min, followed by (B) spray coating of the GO + VC mixed solution.
(C) After an additional 15 min of baking at 150°C, the GO + VC films are reduced into conductive VC-rGO films. Bottom panels show the reduction process on glass slides and parylene-C-encapsulated μECoG arrays pre-patterned in Au on a Si wafer. The transition in color of the GO + VC films from a light brown in panel (B), to a dark black in panel (C), is indicative of GO reduction. Scale bars: 25 mm.

concentration and heating time. We also demonstrate the fabrication and one-step coating process of planar rGO/Au microelectrode arrays encapsulated in parylene-C for microelectrocorticography (μECoG) recordings, cortical stimulation, and neurochemical sensing. *In vitro* characterization of the electrochemical properties of rGO/Au microelectrodes indicates that rGO coatings are stable and significantly enhance the electrode surface area, leading to impedance reduction, as well as charge storage and charge injection capacity increases compared to same-size Au electrodes and other coating materials from literature. The enhanced surface area afforded by the rGO coatings also results in an increase in adsorption site count, enabling the *in vitro* detection of the neurotransmitter dopamine (DA) with a high sensitivity and low detection limit. Finally, to demonstrate the feasibility of rGO/Au μECoG arrays for monitoring microscale neural circuits at high resolution, we show high-density mapping of evoked cortical responses in rat somatosensory cortex from whisker stimulation. Altogether, we demonstrate the potential of VC-reduced rGO coatings as a unique strategy to improve standard electrode technologies, in order to advance future multimodal neural interface applications.

RESULTS AND DISCUSSION

Optimization of the VC reduction method and rGO film characterization

An overview of the VC reduction process is illustrated in Figure 1. The reaction kinetics of VC in water is well established to be of the first-order, and are thus exponentially proportional to the solution temperature (Wang et al., 2017). This implies that VC solutions at room temperature may be used for many days without concerns over material degradation or colloidal instability (De Silva et al., 2017; Wang et al., 2017). Furthermore, when VC is mixed with GO dispersions at room temperature, at least two days of continuous stirring are required before complete reduction of the solution is achieved (Zhang et al., 2010; Abulizi et al., 2014; De Silva et al., 2017). Altogether, this means that it is possible to mix GO and VC, and subsequently form films by directly spray coating GO + VC mixtures onto the target substrate (Figure 1B). The resulting films appear in the characteristic light brown color of GO when dried, and they can then be reduced at any subsequent point in time through a simple heating step. Once the films are heated, they progressively become darker, as a result of the reduction process (Figure 1C and Video S1).

We varied VC concentrations and heating time, and measured the sheet resistance of the resulting film (Figures 2A and 2B). The sheet resistance shows dependence on VC concentration up to 50 mM, and on heating time only up to 15 min at 150°C, beyond which no improvement is observed. Accordingly, at a VC concentration of 50 mM and a heating time of 15 min at 150°C, the optimal sheet resistance of the VC-rGO thin films is 981.50 $\pm$ 125.96 Ω sq^{-1}. From stylus profilometry, the average film thickness is

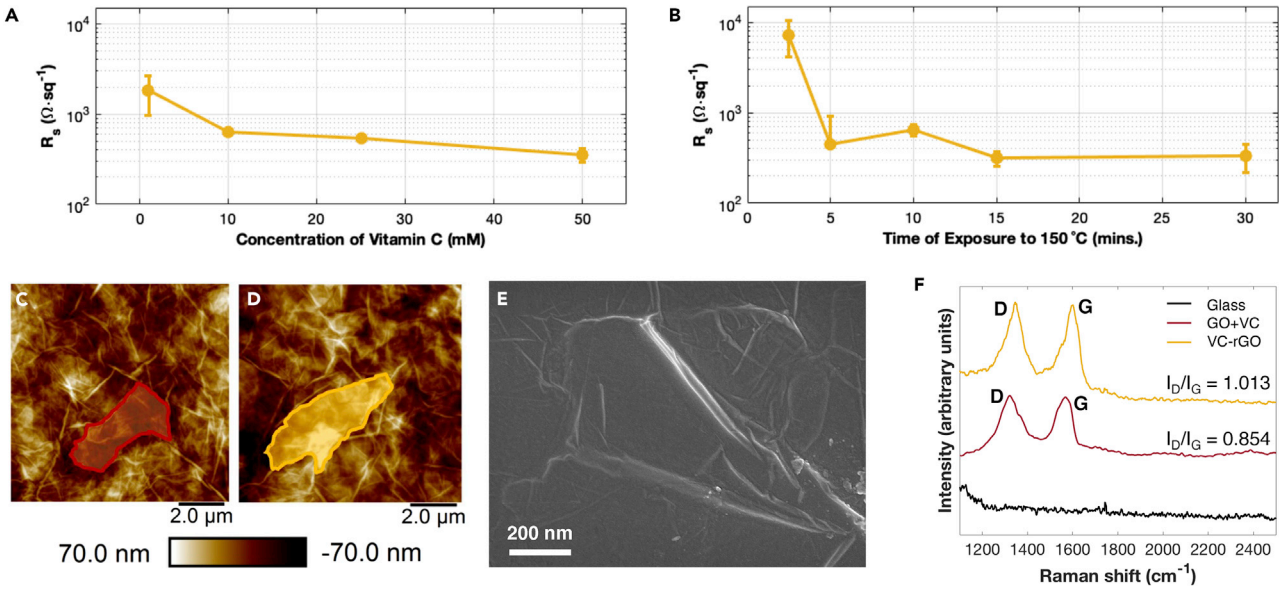

Figure 2. Optimization and characterization of the VC-rGO films

(A and B) Dependence of the dry VC-rGO film sheet resistance on (A) VC concentration and (B) heating time at 150°C (mean ± std. dev., N = 3 samples).

(C and D) AFM of VC-rGO films made using 50 mM VC on glass (C) before and (D) after 15 min of baking at 150°C, showing flake morphology and film roughness.

(E) SEM of a VC-rGO film on glass.

(F) Raman spectra of GO + VC and VC-rGO films on glass, showing the characteristic graphitic peaks in the D and G bands. The I_D/I_G ratio is also provided for each film type.

236.17 ± 26.37 nm, yielding an average DC conductivity of 43.86 ± 4.08 S cm^{-1}. This value is comparable to previous rGO films from VC reduction in solution (Zhang et al., 2010; Fernandez-Merino et al., 2010), and is also higher than some hydrazine-reduced films (Gilje et al., 2007; Wallace et al., 2008). Figure S1 and Table S1 summarize the DC conductivity of rGO films obtained from different published reduction methods (Domingues et al., 2013, Huang et al., 2011, Konios et al., 2015, Li et al., 2008).

AFM of the dried films before (Figure 2C) and after (Figure 2D) the optimized reduction reveals similar flake sizes and distributions, demonstrating that the VC reduction method preserves the structure of the individual graphene flakes. SEM images (Figure 2E) show that individual rGO sheets endow the film with a wrinkled and folded morphology, which contributes to increasing the effective surface area. Finally, Raman spectroscopy (Figure 2F) reveals clear distinctions between the lattice structures of the GO + VC and VC-rGO films. The D band, which is related to the breathing modes of the six-atom carbon lattice, is especially sensitive to edge defects and domain sizes (Stankovich et al., 2007), and thus, the I_D/I_G ratio is a useful measure for distinguishing between GO and rGO films (Kudin et al., 2008; Kaniyoor and Ramaprabhu, 2012; Ferrari and Basko, 2013). Prior to reduction, overlapping graphitic flakes appear as defects in the Raman spectra, and thus there is an initially pronounced D peak, resulting in an I_D/I_G ratio of 0.854 for the GO + VC films. Upon exposure to heat, though, there is extensive reduction of the carbon lattice and removal of oxygen moieties from the GO sheets, resulting in smaller sized domains in which sp^2 vibrations may occur (Stankovich et al., 2007). This, in turn, causes an increase in the intensity of the D band and in the I_D/I_G ratio (1.013) for the VC-rGO films. Given the limited range of the Raman system (180–2,580 cm^{-1}), the 2D and (D + D′) bands do not appear in the spectra, although they are expected in the range of 2,600–3,000 cm^{-1}. However, these peaks show only minor changes in shape or location in response to the reduction step, as has been discussed in previous reports (Kaniyoor and Ramaprabhu, 2012; Muhammad Hafiz et al., 2014).

In addition to the changes in the properties described above, GO + VC films also become more hydrophobic following reduction (Figure S2). For dry GO + VC films, the water contact angle is comparable to bare glass (28.1° ± 0.2° for GO + VC vs. 22.9° ± 1.7° for glass, N = 3 samples). After reduction, the contact angle of the VC-rGO films nearly doubles (45.6° ± 0.7°, N = 3), in agreement with previous studies (Xu et al., 2014; Liu et al., 2015a). The increased hydrophobicity of VC-rGO may result in longer lifetimes for these films in

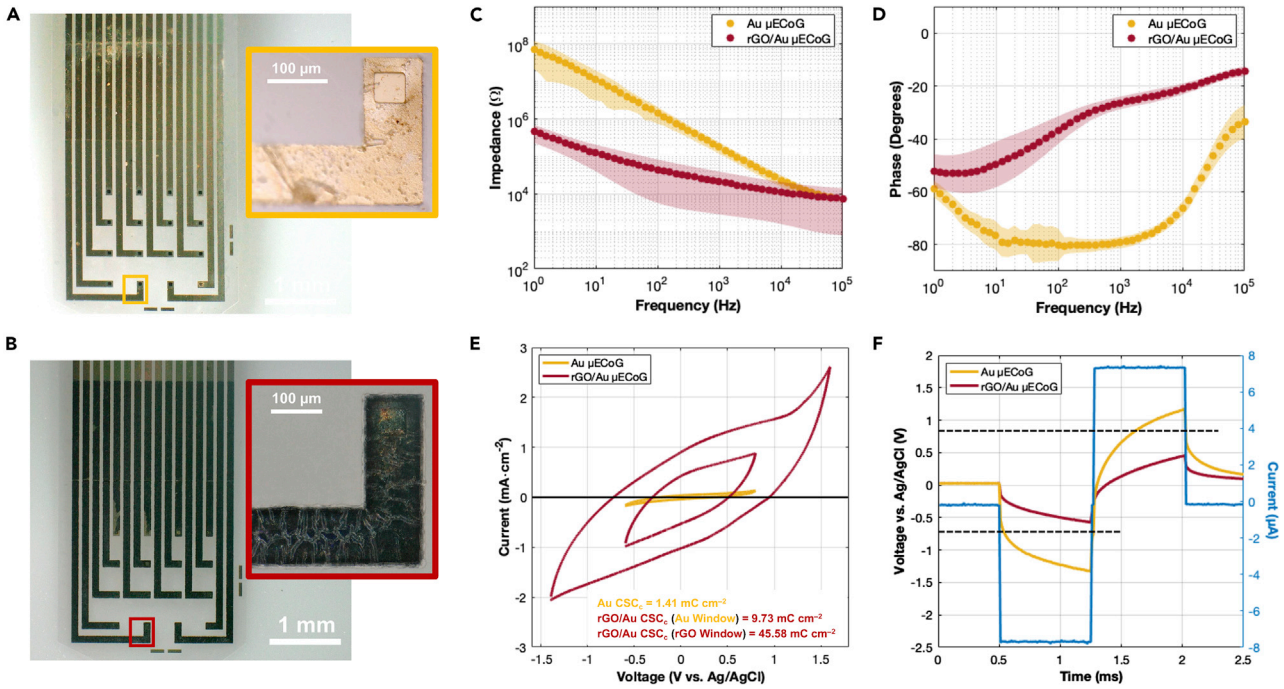

Figure 3. *In vitro* characterization of the rGO/Au μECoG arrays

(A and B) Optical microscopy images of (A) a bare Au and (B) an rGO/Au μECoG array. Insets show an individual channel from each array, including the 50 × 50 μm contact.

(C and D) Bode plots of the impedance (C) modulus and (D) phase for the Au and rGO/Au μECoG arrays. Points are means, shaded regions are std. dev. (N = 3 devices, 48 individual channels total for each electrode type).

(E) Example cyclic voltammograms (CVs) for the Au and rGO/Au μECoG electrodes in the safe operating voltage window of Au (−0.6 V ∼ +0.8 V) and in the full water window of rGO (−1.4 V ∼ +1.6 V). Scan rate, 200 mV s^{-1}. Values of CSC_c are included for each material.

(F) Voltage transients at the Au and rGO/Au μECoG arrays in response to 7.5 μA biphasic current pulses (duration, 650 μs; inter-pulse delay, 20 μs). Black dashed lines denote the water window limits of the Au electrodes.

aqueous environments, such as might be found in living systems. Indeed, a few reports have already highlighted the advantages of hydrophobic carbon nanomaterial coatings to prevent moisture ingress from causing delamination, corrosion, or other failures in both implantable (Zhao et al., 2016) and wearable (Chun et al., 2019) biomedical designs. To further explore this potential benefit in our own work, we evaluated the shelf-life and electrolytic stability of VC-rGO films aged in (i) air, and (ii) 1X PBS at room temperature, over 30 days. Conductivity measurements at the initial and final timepoints (Figure S3) reveal that VC-rGO is highly stable against oxidative degradation in both environments, with the films retaining (93.5 ± 0.8)% and (70.3 ± 3.7)% of their starting conductivity in air and in PBS, respectively (N = 3 samples). This is a significant advantage over alternative coatings—such as PEDOT:PSS, for which conductivity has been shown to decay exponentially with time (Stepien et al., 2017; Kee et al., 2019)—and could be especially advantageous for long-term implants in biological media.

Characterization of rGO/Au and Au μECoG properties *in vitro*

Optical microscopy of the microfabricated Au and rGO/Au μECoG arrays reveals the rougher surface topology following deposition of the VC-rGO coating (Figures 3A and 3B). We observed for all devices that the VC-rGO coating adhered well to the underlying Au layer, and in every instance appeared to be a continuous coating at the exposed contact sites, as well.

The higher degree of surface roughness imparted by the VC-rGO coating results in a reduction of the overall electrode impedance across the 1–10^3 Hz frequency range (Figure 3C). In the higher frequency range (*i.e.*, >10^3 Hz), the Au and rGO/Au microelectrodes behave similarly, which is expected given that this region is dominated by the solution resistance (R_{sol}) and electrode geometric surface area, rather than by material properties (Franks et al., 2005; Boehler et al., 2020). At the reference frequency of 1 kHz, the average impedance of the Au and rGO/Au electrodes are 177.00 ± 8.37 kΩ and 21.12 ± 18.29 kΩ, respectively. With

such a lower impedance, it is expected that the thermal noise in the case of the rGO/Au microelectrodes will be lower than for bare Au electrodes, suggesting an improvement in overall recording quality (Lempka et al., 2011; Scalia et al., 2012). Fitting the impedance to an equivalent circuit model (Table S2 and Figure S4) further reveals that the double-layer capacitance, C_{dl}, of the bare Au electrodes significantly increases by ~400x after rGO coating (Au: C_{dl} = 11.32 ± 0.76 μF cm^{-2} vs. rGO/Au: C_{dl} = 4.40 ± 1.20 mF cm^{-2}, $p < 0.05$). Such increase in C_{dl} can be ascribed to the higher effective surface area, but also to the intrinsically higher capacitance of rGO compared to Au (Piela and Wrona, 1995; Lee et al., 2013). The significantly lower values of R_{ct} observed for the rGO/Au electrodes (Au: 0.180 ± 0. kΩ cm^2 vs. rGO/Au: 0070.035 ± 0.022 kΩ cm^2, $p < 0.05$) suggest that the VC reduction method sufficiently removes excess oxygen terminations from the GO, further improving the charge-transfer characteristics at the VC-rGO layer (Yang and Gunasekaran, 2013).

The increased C_{dl} and enhanced electrochemical surface area of the VC-rGO coatings should also result in a larger area voltammogram for the rGO/Au electrodes, which is indicative of the increased ability to collect and store more charge at the electrode-electrolyte interface (Figures 3E and S5). Indeed, in the water window of Au (−0.6 V ~ +0.8 V) (Ganji et al., 2017b), the CSC_c of uncoated Au electrodes is 1.41 mC cm^{-2}, while for rGO/Au electrodes in the same potential window, the CSC_c is 9.73 mC cm^{-2}. However, when extending the analysis to the full operating window of rGO (−1.4 V ~ +1.6 V), the CSC_c of the rGO/Au electrodes becomes 45.58 mC cm^{-2}, indicating that the VC-rGO coatings considerably increase the charge storage capabilities of bare Au contacts.

Given the greater charge storage capacity of the VC-rGO coatings, it may also be expected that the rGO-coated electrodes should be capable of injecting more charge for stimulation studies compared to uncoated electrodes. From CV, it is possible to calculate the total safe charge injection limit, Q_{inj}, using Equation 1, which represents the total theoretical amount of charge that an electrode can inject, based on the double-layer capacitance and water window limits of the material. The average Q_{inj} of the Au electrodes is 0.016 mC cm^{-2}, compared to 13.20 mC cm^{-2} for the rGO/Au μECoG arrays (Table S3). This ~1000-fold increase in the total safe injection limit is due to the higher C_{dl} of rGO compared to Au, but also follows from the broader rGO potential window compared to most metals. In terms of Q_{inj}, too, the VC-rGO coatings reported here outperform many other standard neural electrode materials, such as IrOx and TiN (Weiland and Humayun, 2014; Kang et al., 2016; Yamagiwa et al., 2015), and approach the higher limits of nanocarbon-based fiber microelectrodes (Apollo et al., 2015; Hejazi et al., 2020a, 2020b) (Table S3).

We have also characterized the electrode charge injection properties using stimulus waveforms more relevant to neural stimulation experiments (Figure 3F). Figure S6 provides an overview of the components that contribute to the polarization potential response in a typical voltage transient experiment (Ganji et al., 2017b; Cisnal et al., 2018; Driscoll et al., 2021), while Figure S7 shows complete voltage transients and CIC evaluation for the Au and rGO/Au μECoG electrodes. In response to 7.5 μA of input current, the bare Au electrodes exceed their safe operating window, reaching polarization potentials greater than ±1 V depending on the current pulse polarity (Figure 3F). In contrast, the rGO/Au electrodes do not exceed ±0.5 V for the same levels of current injection (Figure 3F). Indeed, under the same biphasic pulsing protocol, rGO/Au electrodes can be subjected to currents of up to 15 μA before they exceed their operating window (Figures S7A and S7B). Furthermore, for the bare Au electrodes, the charge injection capacity is CIC = 0.36 ± 0.02 mC cm^{-2}, while for rGO/Au electrodes, CIC = 1.09 ± 0.13 mC cm^{-2} (Table S3 and Figure S7C). The rGO/Au CIC values are comparable to PEDOT:PSS coatings on bare metallic electrodes (Ganji et al., 2017a; Ganji et al., 2017b), as well as hybrid PEDOT:PSS/CNT coatings on Pt (Luo et al., 2011).

Overall, the higher C_{dl}, Q_{inj}, and CIC values, and lower impedance of the rGO/Au electrodes suggest that less power would be consumed by the rGO/Au electrodes in order to maintain the same level of instantaneous electrode current during stimulation experiments (Kelly and Wyatt, 2011; Brunton et al., 2013). VC-rGO coatings also improve the stability of the electrodes under repeated charge injection experiments (Figure S7D). In these tests, we injected continuous biphasic stimulation pulses at 500 μC cm^{-2} phase^{-1} at a frequency of 130 Hz over 24 h, and monitored the impedance every 260,000 pulses (11 million cycles total, 2,808C cm^{-2} phase^{-1} total charge injection). Such injected charge density exceeds the safety limits for Pt-based cochlear implants set by the American National Standards Institute (ANSI, 216 μC cm^{-2} phase^{-1}) (ANSI/AAMI, 2017; Dalrymple et al., 2019), thus representing a very rigorous test

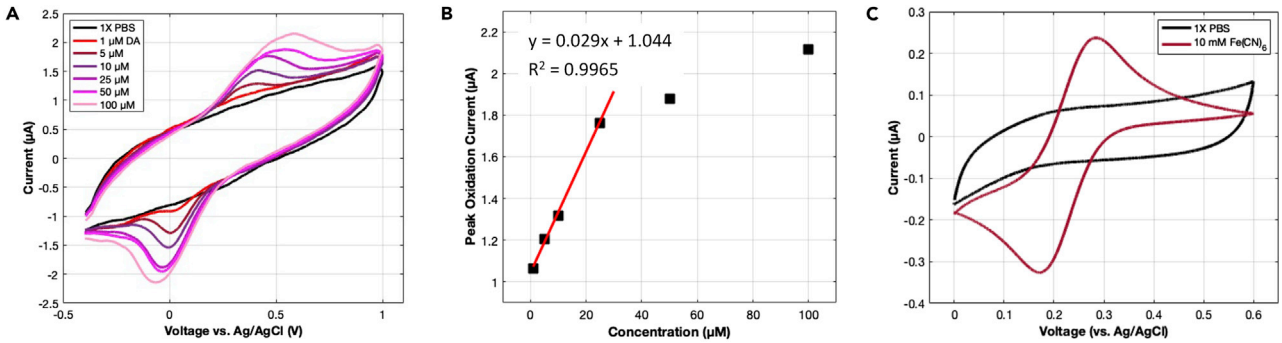

Figure 4. *In vitro* detection of dopamine and ferrocyanide with rGO/Au microelectrodes

(A) CVs at an rGO/Au μECoG in DA-PBS at varying [DA]. Scan rate, 4 V s^{-1}.

(B) The peak oxidation current of the CVs in (A) vs. [DA]. The corresponding equation of best fit and R^2 is included for the linear regime of 1 μM ≤ [DA] < 50 μM.

(C) CVs at an rGO/Au μECoG in 1X PBS and 10 mM $Fe(CN)_6$. Scan rate, 50 mV s^{-1}.

of the electrode coating stability. At the end of the study, the 1 kHz impedance of the bare Au electrodes increased nearly 5x (113 ± 56 kΩ initial, 537 ± 284 kΩ post-injection), whereas continuous charge injection had no effect on the rGO/Au electrodes (initial impedance: 52 ± 10 kΩ, post-injection impedance: 51 ± 16 kΩ). It may be that long-term exposure to such high charge density forced the Au electrodes to operate at voltages outside their safe operating window, causing degradation over time, whereas the rGO-coated electrodes were not driven outside of their much larger water window by the high charge density. The long-term stability of the rGO/Au impedance further suggests that the VC-rGO coating adheres well to the Au surface, and does not delaminate even under severe pulsing conditions. Furthermore, given the stability of the electrochemical impedance, it is likely that the other advantageous properties of the VC-rGO coating, including its CSC_C and CIC, remain largely unchanged, as well.

rGO/Au μECoG arrays for the detection of dopamine

Given the substantial body of literature exploring rGO-coated electrodes for biosensing (Wang et al., 2009; Shao et al., 2010; Wang et al., 2014; Yang et al., 2014; Ng et al., 2015), we also investigated the performance of rGO coatings for DA detection. Figure 4A shows clearly distinguishable oxidation and reduction peaks at the rGO/Au μECoG array for concentrations of DA ([DA]) in the range of 1–100 μM. Note that there is a skewing of the CVs, a drift in the oxidation/reduction peak location, and a change in the peak width depending on [DA]. These phenomena are likely the result of an *iR* drop across the rGO/Au electrodes, caused by both the non-zero spreading resistance of each separate DA solution, as well as the highly capacitive nature of the VC-rGO coating itself (Pajkossy and Mészáros, 2020). Nevertheless, following background subtraction, a calibration curve can be constructed, relating peak oxidation currents to [DA], and showing a linear trend for [DA] < 50 μM (Figure 4B). Above this limit, the linear correlation breaks down due to an increase in DA molecules adsorbed to the electrode surface, leading to a transition from an adsorption-controlled to a diffusion-controlled regime (Venton and Cao, 2020). The fitting equation in the linear range is $i_p = 0.029C + 1.044$ ($R^2 = 0.9965$), where i_p is the peak oxidation current in μA, and C is the concentration in μM. The slope of this fitting curve, $m = 29$ nA μM^{-1}, is the sensitivity of the rGO/Au microelectrodes, while the limit of detection (LOD) is 62.53 ± 16.59 nM (calculated from Equation 2, with a SD of the background signal from the scan in 1X PBS of $s_B = 0.60 \pm 0.16$ nA). It is important to highlight that the LOD here is purely theoretical; the lowest concentration experimentally resolved with the rGO/Au devices was [DA] = 1 μM. Future work will be necessary to explore the experimental LOD of the rGO/Au devices, and confirm that it agrees with the value determined theoretically.

Table S4 provides an overview of some comparable sensors, demonstrating that the rGO/Au electrodes exhibit comparable or better sensitivity than modified glassy carbon electrodes (GCE) (Wang et al., 2014; Thamilselvan et al., 2019), many carbon fiber electrodes (CFEs) (Davis et al., 2020; Hejazi et al., 2020a, 2020b; Patel et al., 2020), and even modified CNTs (Palomäki et al., 2018). In contrast to sensitivity, LODs differ greatly among the various electrode types, but importantly, the LOD of the rGO/Au electrodes here is sufficiently low to support their use for the detection of DA at biologically relevant levels (1 nM–20 μM) (Labib et al., 2016; Palomäki et al., 2018; Matt and Gaskill, 2020; Patel et al., 2020).

By applying the Randles-Sevcik equation (Equation 3), it is also possible to estimate the effective electrochemical surface area of the rGO/Au electrodes, A_{ESA} (Kang et al., 2012; Wang et al., 2014). For this analysis to hold true, it is critical that the reaction considered be a case of reversible outer sphere electron transfer (Ngamchuea et al., 2014; Muhammad et al., 2020), and so the $Fe(CN)_6$ redox event was considered (Figure 4C). Accordingly, we use the value of i_p determined from the CV of $Fe(CN)_6$ at a concentration of 10 mM, as well as the diffusion coefficient $D_{Fe(CN)6} = 7.63 \times 10^{-6}$ cm^2 s^{-1}, which is standard from literature. Under these considerations, the calculated A_{ESA} of the rGO/Au electrodes is 0.0143 mm^2, which corresponds to a ~6x increase in surface area compared to the geometric size of the contact ($GSA = 0.0025$ mm^2). This finding supports the hypothesis that the enhancement of the electrochemistry at the rGO/Au electrode interface compared to uncoated Au arises from the larger effective surface area of the VC-rGO coating. This high area enhancement factor may also indicate that there are more sites for molecules to adsorb to the rGO/Au surface, and since many biomolecules beyond DA—including serotonin (5-HT), glucose, and hydrogen peroxide (H_2O_2)—must adsorb to the electrode surface before they can be detected (Labib et al., 2016), this implies that the rGO/Au electrodes could be useful platforms for biochemical sensing studies involving a wide variety of physiologically relevant species. It will also be important to conduct interference studies in the future, so as to define the selectivity of the rGO/Au microelectrodes toward different species with similar redox potentials (Wang et al., 2014; Yang et al., 2014; Zhang et al., 2017). Looking toward long-term applications, as well, susceptibility to biofouling during DA or other molecule detection will have to be explored (Hanssen et al., 2016)·(Debiemme-Chouvy and Cachet, 2018).

In vivo recording experiments with the rGO/Au μECoG arrays

Finally, to demonstrate the utility of the rGO/Au μECoG arrays for *in vivo* electrophysiology, we conducted a somatosensory evoked potential (SSEP) study in an adult rat (Figure 5). A single whisker was stimulated mechanically with a piezoelectric capillary tube while recording neural activity with the μECoG array across a roughly 750 × 750 μm region of the cerebral cortex sensitive to input from this whisker. Evoked potentials were averaged over 100 separate stimulation presentations, to provide a truly representative mean response for each targeted whisker. Upon whisker stimulation, robust SSEPs (Zhu and Connors, 1999; Luhmann and Khazipov, 2018; Vilarchao et al., 2018) appear across the rGO/Au μECoG array (Figure 5A, left panel). Control recordings subsequently repeated over the same area of cortex with the whisker removed from the capillary tube confirm that the evoked waveforms are not artifacts caused by the whisker stimulation system (Figure 5A, middle panel). Following subtraction of the noise from the SSEPs, we observe clean stimulus-evoked neural activity for each channel of the rGO/Au μECoG array (Figure 5A, right panel), peaking at ~10–15 ms after whisker deflection. This response latency is in excellent agreement with previous reports (Benison et al., 2007; Kheradpezhouh et al., 2017). Furthermore, high-density mapping with the rGO/Au μECoG array evidence a clear spatial gradient in the SSEPs across the sampled area (Figure 5B), with a maximum at the site of the cortical representation for the stimulated whisker (Figure 5C). The distribution of evoked neural activity also clearly shifted in a manner consistent with the cortical representations map when a different whisker was deflected (see Figure S8).

While the *in vitro* impedance of the rGO/Au arrays at 1 kHz is in the range of ~20–80 kΩ, the *in vivo* impedance of the array over vS1 increases to ~50–500 kΩ (Figures S9A and S9B). The lack of correlation between the SSEP amplitudes and the impedance distribution on the array, though, confirms that the spatial organization of the SSEPs reflects the vibrissal cortical whisker representations, and is not dependent on the individual channel impedance ($p = 0.876$ for Stim Trial 1, $p = 0.613$ for Stim Trial 2, Figure S9C). A voltage divider effect due to the 50–500 kΩ electrode impedances in series with the input impedance of the recording system (nominally 16 MΩ at 1 kHz for the Intan RHS system) is expected to produce only about a ~2% difference in signal amplitudes across the array (Nelson et al., 2008). This finding, coupled with the anatomically accurate mapping of SSEP distributions, highlights the advantage of a high-density, microscale array for mapping cortical activity with high spatial resolution.

Conclusion

In this work, we have presented a novel method to enhance the recording, stimulation, and biochemical detection properties of neural microelectrodes using reduced graphene oxide coatings. Specifically, we have demonstrated a novel approach for realizing rGO films that leverages the advantageous kinetics of vitamin C to complete the reduction process in a safer, fully biocompatible, non-destructive, and highly scalable fashion. The VC reduction process is specifically optimized for compatibility with the soft, conformable, polymeric substrates that are commonly used in implantable medical devices. We have also designed the rGO processing and film deposition method for easy integration into microfabrication

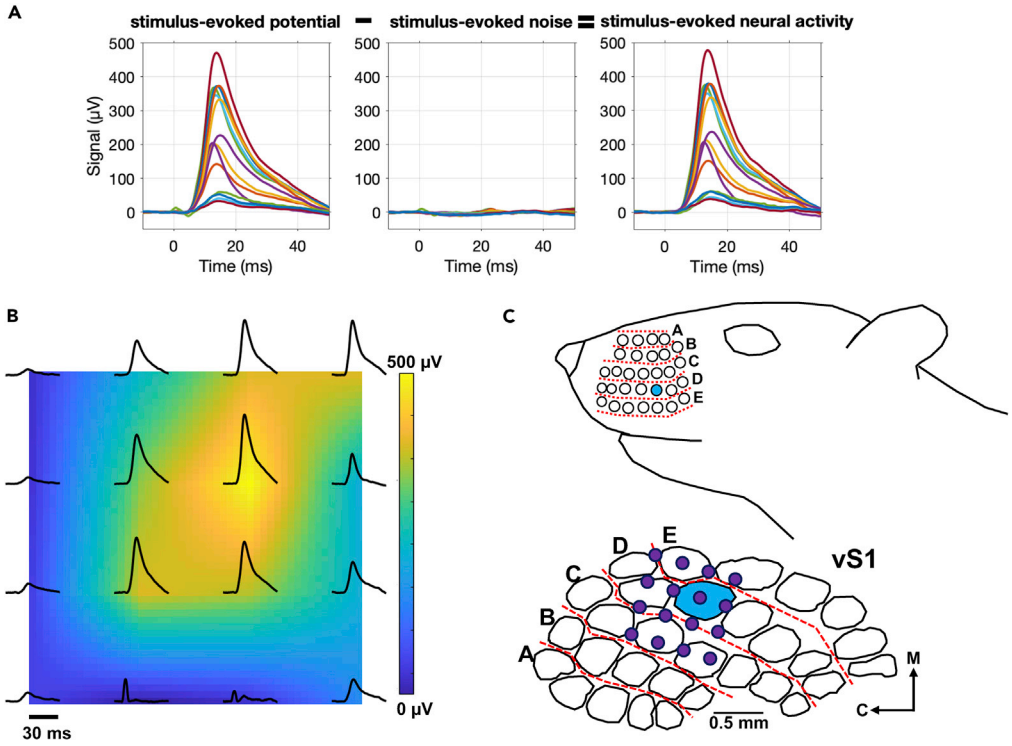

Figure 5. *In vivo* recording with an rGO/Au μECoG array

(A) Left: total evoked potential, middle: noise, right: resulting evoked neural response recorded across an rGO/Au μECoG array. Time on the x axis is relative to onset of mechanical stimulation of a contralateral whisker. Each trace is the mean of 100 evoked responses on each channel, after excluding the 10% largest and 10% smallest responses.

(B) Map of the evoked neural responses on the rGO/Au μECoG array. The colormap represents peak amplitudes of the evoked responses, and overlaid traces show the mean stimulus-evoked response recorded at each channel.

(C) Top: approximate location of the stimulated whisker, highlighted in blue. Bottom: estimated location of the rGO/Au μECoG array relative to the whisker representations in barrel cortex, with the representation corresponding to the stimulated whisker highlighted in blue.

process flows for producing neural microelectrodes. The VC-rGO coatings demonstrated in this work are sufficiently conductive, highly stable, and have significantly improved electrochemical properties over bare metallic electrodes, with values exceeding even PEDOT:PSS and CNT coatings.

The stability of the rGO-coated electrode impedance under continuous charge injection, coupled with the stability of the VC-rGO DC conductivity over time in both air and electrolytic environments, suggests that the VC-rGO films are highly versatile and potentially stable for long-term applications. These findings, along with the excellent charge storage and charge-transfer characteristics, suggest that rGO-coated electrodes are excellent candidates for chronic recording and stimulation studies *in vivo*, although further investigation is required. We have already demonstrated high-density cortical recordings of stimulus-evoked potentials in a rat model, which evidence the ability of this technology to map spatial gradients of neural activity on the microscale. Future work may seek to complete simultaneous recording and stimulation experiments *in vivo* under a similar experimental setup, wherein the rGO/Au arrays may be used not only for recording electrophysiology but also for direct electrical stimulation of neural tissue. We also demonstrated the *in vitro* detection of dopamine using the rGO/Au μECoG arrays with sensitivity of 29 nA μM^{-1} and a limit of detection of 63 nM. These values are comparable to standard electrode technologies used for *in vivo* biochemical studies, such as carbon fiber electrodes, and thus may enable future multimodal experiments involving analytical sensing of biologically relevant chemical species alongside recording and stimulation.

Overall, our novel method of producing rGO coatings relies on the safe and efficient chemical reduction properties of VC. In addition to addressing the safety and polymer compatibility concerns posed by other chemical and thermal reduction processes, the VC reduction method is a biocompatible, readily scalable,

cost-effective procedure to realize rGO films for applications in bioelectronics. Furthermore, the resulting rGO films may serve as an improvement over other complex, time-consuming surface enhancement techniques, resulting in electrode coatings that significantly improve the recording, stimulating, and biochemical sensing properties of electrode interfaces for the nervous system.

Limitations of the study

In this work, we show a scalable and safe process to fabricate rGO-coated neural microelectrodes and demonstrate the feasibility of high-resolution neural recordings *in vivo*, alongside very promising charge delivery and dopamine (DA) sensing performance *in vitro*. Further experiments are needed to characterize stimulation performance and sensitivity for neurochemical sensing *in vivo*. The recording studies in this report were also conducted acutely, so future work ought to explore the chronic stability of these arrays *in vivo*, especially in light of the excellent *in vitro* stability results we discuss. In terms of biosensing, susceptibility of VC-rGO coatings to biofouling, as well as specificity in physiological conditions with multiple interfering chemical species, remain important aspects to be further explored. Additional work will also elucidate the ability of VC-rGO to detect other biologically relevant neurotransmitters and analytes beyond DA, such as serotonin, acetylcholine, and uric acid.

STAR★METHODS

Detailed methods are provided in the online version of this paper and include the following:

- KEY RESOURCES TABLE
- RESOURCE AVAILABILITY
  - Lead contact
  - Materials availability
  - Data and code availability
- EXPERIMENTAL MODEL AND SUBJECT DETAILS
- METHOD DETAILS
  - Preparation of GO + VC solutions
  - Spray-coating techniques
  - Film characterization
  - Monitoring the DC conductivity over 1 month
  - Fabrication of μECoG devices
  - Characterization of μECoG devices *in vitro*
  - Fitting procedures for μECoG devices in 1X PBS
  - Evaluating the total charge injection capacity
  - Dopamine and ferrocyanide detection *in vitro*
- QUANTIFICATION AND STATISTICAL ANALYSIS

SUPPLEMENTAL INFORMATION

Supplemental information can be found online at https://doi.org/10.1016/j.isci.2022.104652.

ACKNOWLEDGMENTS

This work was supported by the National Science Foundation Graduate Research Fellowship Program (NSF GRP) grant No. DGE-1845298 (B.B.M.), the National Institutes of Health (NIH) grants No. K12HD073945, R01NS121219 (F.V.), and T32NS091006 (N.V.A.), and by the Linda Pechenik Award (F.V.). This work was performed in part at the University of Pennsylvania Singh Center for Nanotechnology, an NNCI member supported by NSF Grant ECCS-154253. Any opinions, findings, and conclusions or recommendations expressed in this material are those of the authors, and do not necessarily reflect the views of the NIH or NSF.

AUTHOR CONTRIBUTIONS

Conceptualization, B.B.M., N.V.A., and F.V.; Methodology, B.B.M., N.V.A., P.U., A.G.R., and F.V.; Investigation, B.B.M., N.V.A., P.U., T.P., N.P.-R., Q.H., F.C., and A.G.R.; Writing – Original Draft, B.B.M., N.V.A., and F.V.; Writing – Review & Editing, B.B.M., N.V.A., P.U., T.P., N.P.-R., Q.H., F.C., A.G.R., and F.V.; Funding Acquisition, A.G.R. and F.V.; Resources, A.G.R. and F.V.; Supervision, F.V.

DECLARATION OF INTERESTS

The authors declare no conflict of interests.

Received: April 13, 2022
Revised: May 28, 2022
Accepted: June 16, 2022
Published: July 15, 2022

REFERENCES

Abulizi, A., Okitsu, K., and Zhu, J.J. (2014). Ultrasound assisted reduction of graphene oxide to graphene in l-ascorbic acid aqueous solutions: kinetics and effects of various factors on the rate of graphene formation. Ultrason. Sonochem. *21*, 1174–1181. https://doi.org/10.1016/j.ultsonch.2013.10.019.

Alazmi, A., Rasul, S., Patole, S.P., and Costa, P.M. (2016). Comparative study of synthesis and reduction methods for graphene oxide. Polyhedron *116*, 153–161. https://doi.org/10.1016/j.poly.2016.04.044.

ANSI/AAMI (2017). CI86:2017 Cochlear Implant Systems: Requirements for Safety, Functional Verification, Labelling and Reliability Reporting (Association for the Advancement of Medical Instrumentation (AAMI)).

Apollo, N.V., Maturana, M.I., Tong, W., Nayagam, D.A.X., Shivdasani, M.N., Foroughi, J., Wallace, G.G., Prawer, S., Ibbotson, M.R., and Garrett, D.J. (2015). Soft, flexible freestanding neural stimulation and recording electrodes fabricated from reduced graphene oxide. Adv. Funct. Mater. *25*, 3551–3559. https://doi.org/10.1002/adfm.201500110.

Aqrawe, Z., Wright, B., Patel, N., Vyas, Y., Malmstrom, J., Montgomery, J.M., Williams, D., Travas-Sejdic, J., and Svirskis, D. (2019). The influence of macropores on PEDOT/PSS microelectrode coatings for neuronal recording and stimulation. Sens. Actuators: B. Chem. *281*, 549–560. https://doi.org/10.1016/j.snb.2018.10.099.

Aregueta-Robles, U.A., Woolley, A.J., Poole-Warren, L.A., Lovell, N.H., and Green, R.A. (2014). Organic electrode coatings for next-generation neural interfaces. Front. Neuroeng. *7*, 15. https://doi.org/10.3389/fneng.2014.00015.

Becerril, H.A., Mao, J., Liu, Z., Stoltenberg, R.M., Bao, Z., and Chen, Y. (2008). Evaluation of solution-processed reduced graphene oxide films as transparent conductors. ACS Nano *2*, 463–470. https://doi.org/10.1021/nn700375n.

Behler, K.D., Stravato, A., Mochalin, V., Korneva, G., Yushin, G., and Gogotsi, Y. (2009). Nanodiamond-polymer composite fibers and coatings. ACS Nano *3*, 363–369. https://doi.org/10.1021/nn800445z.

Benison, A.M., Rector, D.M., and Barth, D.S. (2007). Hemispheric mapping of secondary somatosensory cortex in the rat. J. Neurophysiol. *97*, 200–207. https://doi.org/10.1152/jn.00673.2006.

Bera, B., Kar, T., Chakraborty, A., and Neergat, M. (2017). Influence of nitrogen-doping in carbon on equivalent distributed resistance and capacitance – implications to electrocatalysis of oxygen reduction reaction. J. Electroanal. Chem. *805*, 184–192. https://doi.org/10.1016/j.jelechem.2017.10.025.

Boehler, C., Carli, S., Fadiga, L., Stieglitz, T., and Asplund, M. (2020). Tutorial: guidelines for standardized performance tests for electrodes intended for neural interfaces and bioelectronics. Nat. Protoc. *15*, 3557–3578. https://doi.org/10.1038/s41596-020-0389-2.

Brunton, E.K., Rajan, R., and Lowery, A.J. (2013). Optimising electrode surface area to minimize power consumption in a cortical penetrating prosthesis. In International IEEE/EMBS Conference on Neural Engineering, NER (IEEE), pp. 1477–1480. https://doi.org/10.1109/NER.2013.6696224.

Castagnola, E., Biso, M., and Ricci, D. (2009). Controlled electrochemical polypyrrole and carbon nanotube Co-deposition onto platinum electrodes. In 9th IEEE Conference on Nanotechnology (IEEE-NANO) (IEEE), pp. 842–845.

Castagnola, V., Descamps, E., Lecestre, A., Dahan, L., Remaud, J., Nowak, L., and Bergaud, C. (2015). Parylene-based flexible neural probes with PEDOT coated surface for brain stimulation and recording. Biosens. Bioelectron. *67*, 450–457. https://doi.org/10.1016/j.bios.2014.09.004.

Chen, Y., Fu, K., Zhu, S., Luo, W., Wang, Y., Li, Y., Hitz, E., Yao, Y., Dai, J., Wan, J., et al. (2016). Reduced graphene oxide films with ultrahigh conductivity as Li-ion battery current collectors. Nano Lett. *16*, 3616–3623. https://doi.org/10.1021/acs.nanolett.6b00743.

Chun, S., Son, W., Kim, D.W., Lee, J., Min, H., Jung, H., Kwon, D., Kim, A.H., Kim, Y.J., Lim, S.K., et al. (2019). Water-Resistant and skin-adhesive wearable electronics using graphene fabric sensor with octopus-inspired microsuckers. ACS Appl. Mater. Interfaces *11*, 16951–16957. https://doi.org/10.1021/acsami.9b04206.

Chung, S., and Park, S. (2013). Effects of temperature on mechanical properties of SU-8 photoresist material. J. Mech. Sci. Technol. *27*, 2701–2707. https://doi.org/10.1007/s12206-013-0714-6.

Cisnal, A., Fraile, J.C., Pérez-Turiel, J., Muñoz-Martinez, V., Müller, C., and R. Ihmig, F. (2018). A measurement setup and automated calculation method to determine the charge injection capacity of implantable microelectrodes. Sensors *18*. https://doi.org/10.3390/s18124152.

Cogan, S.F. (2008). Neural stimulation and recording electrodes. Annu. Rev. Biomed. Eng. *10*, 275–309. https://doi.org/10.1146/annurev.bioeng.10.061807.160518.

Cui, X.T., and Zhou, D.D. (2007). Poly(3, 4-ethylenedioxythiophene) for chronic neural stimulation. IEEE Trans. Neural Syst. Rehabil. Eng. *15*, 502–508. https://doi.org/10.1109/TNSRE.2007.909811.

Dalrymple, A.N., Huynh, M., Robles, U.A., Marroquin, J.B., Lee, C.D., Petrossians, A., Whalen, J.J., Li, D., Parkington, H.C., Forsythe, J.S., et al. (2019). Electrochemical and mechanical performance of reduced graphene oxide , conductive hydrogel , and electrodeposited Pt – Ir coated electrodes : an active in vitro study. J. Neural. Eng. *17*, 016015. https://doi.org/10.1088/1741-2552/ab5163.

Davis, S.E., Korich, A.L., and Ramsson, E.S. (2020). Enhancement of fast scan cyclic voltammetry detection of dopamine with tryptophan-modified electrodes. PLoS One *15*, e0235407. https://doi.org/10.1371/journal.pone.0235407.

De Silva, K.K.H., Huang, H.H., Joshi, R., and Yoshimura, M. (2017). Chemical reduction of graphene oxide using green reductants. Carbon *119*, 190–199. https://doi.org/10.1016/j.carbon.2017.04.025.

Debiemme-Chouvy, C., and Cachet, H. (2018). Electrochemical (pre)treatments to prevent biofouling. Curr. Opin. Electrochem. *11*, 48–54. https://doi.org/10.1016/j.coelec.2018.07.006.

Dine-Hart, R.A., Parker, D.B.V., and Wright, W.W. (1971). Oxidative degradation of a polyimide film: III. Kinetic studies. Br. Polym. J. *3*, 235–236. https://doi.org/10.1002/pi.4980030506.

Ding, H., Zhang, S., Chen, J.T., Hu, X.P., Du, Z.F., Qiu, Y.X., and Zhao, D.L. (2015). Reduction of graphene oxide at room temperature with vitamin C for RGO – TiO 2 photoanodes in dye-sensitized solar cell. Thin Solid Films *584*, 29–36. https://doi.org/10.1016/j.tsf.2015.02.038.

Domingues, S.H., Kholmanov, I.N., Kim, T., Kim, J., Tan, C., Chou, H., Alieva, Z.A., Piner, R., Zarbin, A.J., and Ruoff, R.S. (2013). Reduction of graphene oxide films on Al foil for hybrid transparent conductive film applications. Carbon *63*, 454–459. https://doi.org/10.1016/j.carbon.2013.07.007.

Driscoll, N., Maleski, K., Richardson, A.G., Murphy, B., Anasori, B., Lucas, T.H., Gogotsi, Y., and Vitale, F. (2020). Fabrication of Ti3C2 MXene microelectrode arrays for in vivo neural recording. J. Vis. Exp. *15*, e60741. https://doi.org/10.3791/60741.

Driscoll, N., Erickson, B., Murphy, B.B., Richardson, A.G., Robbins, G., Apollo, N.V.,

Mentzelopoulos, G., Mathis, T., Hantanasirisakul, K., Bagga, P., et al. (2021). MXene-infused bioelectronic interfaces for multiscale electrophysiology and stimulation. Sci. Transl. Med. *13*. https://doi.org/10.1126/scitranslmed.abf8629.

Dua, V., Surwade, S., Ammu, S., Agnihotra, S., Jain, S., Roberts, K., Park, S., Ruoff, R., and Manohar, S. (2010). All-organic vapor sensor using inkjet-printed reduced graphene oxide. Angew. Chem., Int. Ed. Engl. *49*, 2154–2157. https://doi.org/10.1002/anie.200905089.

Eda, G., Fanchini, G., and Chhowalla, M. (2008). Large-area ultrathin films of reduced graphene oxide as a transparent and flexible electronic material. Nat. Nanotechnol. *3*, 270–274. https://doi.org/10.1038/nnano.2008.83.

Elgrishi, N., Rountree, K.J., McCarthy, B.D., Rountree, E.S., Eisenhart, T.T., and Dempsey, J.L. (2018). A practical beginner's guide to cyclic voltammetry. J. Chem. Educ. *95*, 197–206. https://doi.org/10.1021/acs.jchemed.7b00361.

Espinoza, E.M., Clark, J.A., Soliman, J., Derr, J.B., Morales, M., and Vullev, V.I. (2019). Practical aspects of cyclic voltammetry: how to estimate reduction potentials when irreversibility prevails. J. Electrochem. Soc. *166*, H3175–H3187. https://doi.org/10.1149/2.0241905jes.

Fang, J., Xie, Z., Wallace, G., and Wang, X. (2017). Co-deposition of carbon dots and reduced graphene oxide nanosheets on carbon-fiber microelectrode surface for selective detection of dopamine. Appl. Surf. Sci. *412*, 131–137. https://doi.org/10.1016/j.apsusc.2017.03.257.

Feng, J., Li, Q., Cai, J., Yang, T., Chen, J., and Hou, X. (2019). Electrochemical detection mechanism of dopamine and uric acid on titanium nitride-reduced graphene oxide composite with and without ascorbic acid. Sens. Actuators, B *298*, 126872. https://doi.org/10.1016/j.snb.2019.126872.

Fernández-Merino, M.J., Guardia, L., Paredes, J.I., Villar-Rodil, S., Solís-Fernández, P., Martínez-Alonso, A., and Tascón, J.M.D. (2010). Vitamin C is an ideal substitute for hydrazine in the reduction of graphene oxide suspensions. J. Phys. Chem. C *114*, 6426–6432. https://doi.org/10.1021/jp100603h.

Fernández-Merino, M., Paredes, J., Villar-Rodil, S., Guardia, L., Solís-Fernández, P., Salinas-Torres, D., Cazorla-Amorós, D., Morallón, E., Martínez-Alonso, A., and Tascón, J. (2012). Investigating the influence of surfactants on the stabilization of aqueous reduced graphene oxide dispersions and the characteristics of their composite films. Carbon *50*, 3184–3194. https://doi.org/10.1016/j.carbon.2011.10.039.

Ferrari, A.C., and Basko, D.M. (2013). Raman spectroscopy as a versatile tool for studying the properties of graphene. Nat. Nanotechnol. *8*, 235–246. https://doi.org/10.1038/NNANO.2013.46.

Franks, W., Schenker, I., Schmutz, P., and Hierlemann, A. (2005). Impedance characterization and modeling of electrodes for biomedical applications. IEEE Trans. Biomed. Eng. *52*, 1295–1302. https://doi.org/10.1109/TBME.2005.847523.

Ganji, M., Elthakeb, A.T., Tanaka, A., Gilja, V., Halgren, E., and Dayeh, S.A. (2017a). Scaling effects on the electrochemical performance of poly (3, 4-ethylenedioxythiophene (PEDOT), Au, and Pt for electrocorticography recording. Adv. Funct. Mater. *27*, 1703018. https://doi.org/10.1002/adfm.201703018.

Ganji, M., Tanaka, A., Gilja, V., Halgren, E., and Dayeh, S.A. (2017b). Scaling effects on the electrochemical stimulation performance of Au , Pt , and PEDOT : PSS electrocorticography arrays. Adv. Funct. Mater. *27*, 1703019. https://doi.org/10.1002/adfm.201703019.

Gilje, S., Han, S., Wang, M., Wang, K.L., and Kaner, R.B. (2007). A chemical route to graphene for device applications. Nano Lett. *7*, 3394–3398. https://doi.org/10.1021/nl0717715.

Goel, P., Möller, M., and Weichold, O. (2009). Generation of anisotropic conductivity in polymer films using localized microvoids formed by solvent crazing as nanoreactors. Chem. Mater. *21*, 3036–3038. https://doi.org/10.1021/cm900987f.

Green, R.A., Hassarati, R.T., Bouchinet, L., Lee, C.S., Cheong, G.L., Yu, J.F., Dodds, C.W., Suaning, G.J., Poole-Warren, L.A., and Lovell, N.H. (2012). Substrate dependent stability of conducting polymer coatings on medical electrodes. Biomaterials *33*, 5875–5886. https://doi.org/10.1016/j.biomaterials.2012.05.017.

Hanssen, B.L., Siraj, S., and Wong, D.K.Y. (2016). Recent strategies to minimise fouling in electrochemical detection systems. Rev. Anal. Chem. *35*, 1–28. https://doi.org/10.1515/revac-2015-0008.

Harder, T.A., Yao, T.J., He, Q., Shih, C.Y., and Tai, Y.C. (2002). Residual stress in thin-film parylene-C. In MEMS 2002 IEEE International Conference (IEEE), pp. 435–438. https://doi.org/10.1109/MEMSYS.2002.984296.

Harris, A.R., Morgan, S.J., Chen, J., Kapsa, R.M.I., Wallace, G.G., and Paolini, A.G. (2013). Conducting polymer coated neural recording electrodes. J. Neural. Eng. *10*, 016004. https://doi.org/10.1088/1741-2560/10/1/016004.

Hejazi, M.A., Tong, W., Stacey, A., Sun, S.H., Yunzab, M., Almasi, A., Jung, Y.J., Meffin, H., Fox, K., Edalati, K., et al. (2020a). High fidelity bidirectional neural interfacing with carbon fiber microelectrodes coated with boron-doped carbon nanowalls : an acute study. Adv. Funct. Mater. *30*, 2006101. https://doi.org/10.1002/adfm.202006101.

Hejazi, M.A., Tong, W., Stacey, A., Soto-Breceda, A., Ibbotson, M.R., Yunzab, M., Maturana, M.I., Almasi, A., Jung, Y.J., Sun, S., et al. (2020b). Hybrid diamond/carbon fiber microelectrodes enable multimodal electrical/chemical neural interfacing. Biomaterials *230*, 119648. https://doi.org/10.1016/j.biomaterials.2019.119648.

Hirschorn, B., Orazem, M.E., Tribollet, B., Vivier, V., Frateur, I., and Musiani, M. (2010). Determination of effective capacitance and film thickness from constant-phase-element parameters. Electrochim. Acta *55*, 6218–6227. https://doi.org/10.1016/j.electacta.2009.10.065.

Huang, L., Liu, Y., Ji, L.C., Xie, Y.Q., Wang, T., and Shi, W.Z. (2011). Pulsed laser assisted reduction of graphene oxide. Carbon *49*, 2431–2436. https://doi.org/10.1016/j.carbon.2011.01.067.

Salavagione, H.J., Sherwood, J., De bruyn, M., Budarin, V.L., Ellis, G.J., Clark, J.H., and Shuttleworth, P.S. (2017). Identification of high performance solvents for the sustainable processing of graphene. Green Chem. *19*, 2550–2560. https://doi.org/10.1039/c7gc00112f.

Kahouli, A., Sylvestre, A., Ortega, L., Jomni, F., Yangui, B., Maillard, M., Berge, B., Robert, J.C., and Legrand, J. (2014). Structural and dielectric study of parylene C thin films. Appl. Phys. Lett. *94*, 152901. https://doi.org/10.1063/1.3114404.

Kang, J., Kim, T., Tak, Y., Lee, J.H., and Yoon, J. (2012). Cyclic voltammetry for monitoring bacterial attachment and biofilm formation. J. Ind. Eng. Chem. *18*, 800–807. https://doi.org/10.1016/j.jiec.2011.10.002.

Kang, X., Liu, J., Tian, H., Yang, B., NuLi, Y., and Yang, C. (2016). Sputtered iridium oxide modified flexible parylene microelectrodes array for electrical recording and stimulation of muscles. Sens. Actuators, B *225*, 267–278. https://doi.org/10.1016/j.snb.2015.11.050.

Kaniyoor, A., and Ramaprabhu, S. (2012). A Raman spectroscopic investigation of graphite oxide derived graphene. AIP Adv. *2*, 032183. https://doi.org/10.1063/1.4756995.

Kee, S., Kim, H., Paleti, S.H.K., El Labban, A., Neophytou, M., Emwas, A.H., Alshareef, H.N., and Baran, D. (2019). Highly stretchable and air-stable PEDOT:PSS/ionic liquid composites for efficient organic thermoelectrics. Chem. Mater. *31*, 3519–3526. https://doi.org/10.1021/acs.chemmater.9b00819.

Keefer, E.W., Botterman, B.R., Romero, M.I., Rossi, A.F., and Gross, G.W. (2008). Carbon nanotube coating improves neuronal recordings. Nat. Nanotechnol. *3*, 434–439. https://doi.org/10.1038/nnano.2008.174.

Kellis, S., Sorensen, L., Darvas, F., Sayres, C., O'Neill, K., Brown, R.B., House, P., Ojemann, J., and Greger, B. (2016). Multi-scale analysis of neural activity in humans: implications for micro-scale electrocorticography. Clin. Neurophysiol. *127*, 591–601. https://doi.org/10.1016/j.clinph.2015.06.002.

Kelly, S.K., and Wyatt, J.L. (2011). A power-efficient neural tissue stimulator with energy recovery. IEEE Trans. Biomed. Circuits Syst. *5*, 20–29. https://doi.org/10.1109/TBCAS.2010.2076384.

Khan, R.K., Farghaly, A.A., Silva, T.A., Ye, D., and Collinson, M.M. (2019). Gold-nanoparticle-decorated titanium nitride electrodes prepared by glancing-angle deposition for sensing applications. ACS Appl. Nano Mater. *2*, 1562–1569. https://doi.org/10.1021/acsanm.8b02354.

Kheradpezhouh, E., Adibi, M., and Arabzadeh, E. (2017). Response dynamics of rat barrel cortex neurons to repeated sensory stimulation. Sci. Rep. *7*, 11445. https://doi.org/10.1038/s41598-017-11477-6.

Khodagholy, D., Gelinas, J.N., Thesen, T., Doyle, W., Devinsky, O., Malliaras, G.G., and Buzsáki, G. (2015). NeuroGrid: recording action potentials

from the surface of the brain. Nat. Neurosci. *18*, 310–315. https://doi.org/10.1038/nn.3905.

Kochowski, S., and Nitsch, K. (2002). Description of the frequency behavior of metal – SiO 2 – GaAs structure characteristics by electrical equivalent circuit with constant phase element. Thin Solid Films *415*, 133–137. https://doi.org/10.1016/S0040-6090(02)00506-0.

Kolarcik, C.L., Catt, K., Rost, E., Albrecht, I.N., Bourbeau, D., Du, Z., Kozai, T.D.Y., Luo, X., Weber, D.J., and Tracy Cui, X. (2014). Evaluation of poly (3, 4-ethylenedioxythiophene)/carbon nanotube neural electrode coatings for stimulation in the dorsal root ganglion. J. Neural. Eng. *12*, 016008. https://doi.org/10.1088/1741-2560/12/1/016008.

Konios, D., Petridis, C., Kakavelakis, G., Sygletou, M., Savva, K., Stratakis, E., and Kymakis, E. (2015). Reduced graphene oxide micromesh electrodes for large area, flexible, organic photovoltaic devices. Adv. Funct. Mater. *25*, 2213–2221. https://doi.org/10.1002/adfm.201404046.

Kostarelos, K., Bianco, A., and Prato, M. (2009). Promises, facts and challenges for carbon nanotubes in imaging and therapeutics. Nat. Nanotechnol. *4*, 627–633. https://doi.org/10.1038/nnano.2009.241.

Kudin, K.N., Ozbas, B., Schniepp, H.C., Prud'homme, R.K., Aksay, I.A., and Car, R. (2008). Raman spectra of graphite oxide and functionalized graphene sheets. Nano Lett. *8*, 36–41. https://doi.org/10.1021/nl071822y.

Labib, M., Sargent, E.H., and Kelley, S.O. (2016). Electrochemical methods for the analysis of clinically relevant biomolecules. Chem. Rev. *116*, 9001–9090. https://doi.org/10.1021/acs.chemrev.6b00220.

Laurila, T., Sainio, S., and Caro, M.A. (2017). Hybrid carbon based nanomaterials for electrochemical detection of biomolecules. Prog. Mater. Sci. *88*, 499–594. https://doi.org/10.1016/j.pmatsci.2017.04.012.

Lee, Y.H., Chang, K., Hu, C.C., and Hu, C. (2013). Differentiate the pseudocapacitance and double-layer capacitance contributions for nitrogen-doped reduced graphene oxide in acidic and alkaline electrolytes. J. Power Sources *227*, 300–308. https://doi.org/10.1016/j.jpowsour.2012.11.026.

Lempka, S.F., Johnson, M.D., Moffitt, M.A., Otto, K.J., Kipke, D.R., and McIntyre, C.C. (2011). Theoretical analysis of intracortical microelectrode recordings. J. Neural. Eng. *8*, 045006. https://doi.org/10.1088/1741-2560/8/4/045006.

Li, D., Müller, M.B., Gilje, S., Kaner, R.B., and Wallace, G.G. (2008). Processable aqueous dispersions of graphene nanosheets. Nat. Nanotechnol. *3*, 101–105. https://doi.org/10.1038/nnano.2007.451.

Lin, J.C., Lin, J.C.H., Deng, P., Lam, G., Lu, B., Lee, Y.K., and Tai, Y.C. (2011). Creep of parylene-C film. In 2011 16th International Solid-State Sensors, Actuators and Microsystems Conference (IEEE), pp. 2698–2701. https://doi.org/10.1109/TRANSDUCERS.2011.5969483.

Lin, X., Jia, J., Yousefi, N., Shen, X., and Kim, J.K. (2013). Excellent optoelectrical properties of graphene oxide thin films deposited on a flexible substrate by Langmuir–Blodgett assembly. J. Mater. Chem. C *1*, 6869. https://doi.org/10.1039/c3tc31497a.

Liu, H., Wang, H., and Zhang, X. (2015a). Facile fabrication of freestanding ultrathin reduced graphene oxide membranes for water purification. Adv. Mater. *27*, 249–254. https://doi.org/10.1002/adma.201404054.

Liu, T.-C., Chuang, M.C., Chu, C.Y., Huang, W.C., Lai, H.Y., Wang, C.T., Chu, W.L., Chen, S.Y., and Chen, Y.Y. (2015b). Implantable graphene-based neural electrode interfaces for electrophysiology and neurochemistry in in vivo hyperacute stroke model. ACS Appl. Mater. Interfaces *8*, 187–196. https://doi.org/10.1021/acsami.5b08327.

Ludwig, K.A., Langhals, N.B., Joseph, M.D., Richardson-Burns, S.M., Hendricks, J.L., and Kipke, D.R. (2011). Poly(3, 4-ethylenedioxythiophene) (PEDOT) polymer coatings facilitate smaller neural recording electrodes. J. Neural. Eng. *8*, 014001. https://doi.org/10.1088/1741-2560/8/1/014001.

Luhmann, H.J., and Khazipov, R. (2018). Neuronal activity patterns in the developing barrel cortex. Neuroscience *368*, 256–267. https://doi.org/10.1016/j.neuroscience.2017.05.025.

Luo, X., Weaver, C.L., Zhou, D.D., Greenberg, R., and Cui, X.T. (2011). Highly stable carbon nanotube doped poly (3, 4-ethylenedioxythiophene) for chronic neural stimulation. Biomaterials *32*, 5551–5557. https://doi.org/10.1016/j.biomaterials.2011.04.051.

Manbohi, A., and Ahmadi, S.H. (2019). Sensitive and selective detection of dopamine using electrochemical microfluidic paper-based analytical nanosensor. Sens. Bio-Sensing Res. *23*, 100270. https://doi.org/10.1016/j.sbsr.2019.100270.

Matt, S.M., and Gaskill, P.J. (2020). Where is dopamine and how do immune cells see it?: dopamine-mediated immune cell function in health and disease. J. Neuroimmune Pharmacol. *15*, 114–164. https://doi.org/10.1007/s11481-019-09851-4.

Muhammad Hafiz, S., Ritikos, R., Whitcher, T.J., Md. Razib, N., Bien, D.C.S., Chanlek, N., Nakajima, H., Saisopa, T., Songsiriritthigul, P., Huang, N.M., and Rahman, S.A. (2014). A practical carbon dioxide gas sensor using room-temperature hydrogen plasma reduced graphene oxide. Sens. Actuators, B *193*, 692–700. https://doi.org/10.1016/j.snb.2013.12.017.

Muhammad, S., Ummul Banin Zahra, U.B.Z., Aneela Ahmad, A.A., Shah, L.A., and Muhammad, A. (2020). Understanding the basics of electron transfer and cyclic voltammetry of potassium ferricyanide - an outer sphere heterogeneous electrode reaction. J. Chem. Soc. Pakistan *42*, 813. https://doi.org/10.52568/000705/jcsp/42.06.2020.

Murphy, B.B., Mulcahey, P.J., Driscoll, N., Richardson, A.G., Robbins, G.T., Apollo, N.V., Maleski, K., Lucas, T.H., Gogotsi, Y., Dillingham, T., and Vitale, F. (2020). A gel-free $Ti_3C_2T_x$ -based electrode array for high-density, high-resolution surface electromyography. Adv. Mater. Technol. *5*, 2000325. https://doi.org/10.1002/admt.202000325.

Nelson, M.J., Pouget, P., Nilsen, E.A., Patten, C.D., and Schall, J.D. (2008). Review of signal distortion through metal microelectrode recording circuits and filters. J. Neurosci. Methods *169*, 141–157. https://doi.org/10.1016/j.jneumeth.2007.12.010.

Ng, A.M.H., Teck Lim, C., Low, H.Y., and Loh, K.P. (2015). Highly sensitive reduced graphene oxide microelectrode array sensor. Biosens. Bioelectron. *65*, 265–273. https://doi.org/10.1016/j.bios.2014.10.048.

Ngamchuea, K., Eloul, S., Tschulik, K., and Compton, R.G. (2014). Planar diffusion to macro disc electrodes—what electrode size is required for the Cottrell and Randles-Sevcik equations to apply quantitatively? J. Solid State Electrochem. *18*, 3251–3257. https://doi.org/10.1007/s10008-014-2664-z.

Ning, J., Wang, J., Li, X., Qiu, T., Luo, B., Hao, L., Liang, M., Wang, B., and Zhi, L. (2014). A fast room-temperature strategy for direct reduction of graphene oxide films towards flexible transparent conductive films. J. Mater. Chem. A *2*, 10969–10973. https://doi.org/10.1039/c4ta00527a.

Pajkossy, T., and Mészáros, G. (2020). Connection of CVs and impedance spectra of reversible redox systems, as used for the validation of a dynamic electrochemical impedance spectrum measurement system. J. Solid State Electrochem. *24*, 2883–2889. https://doi.org/10.1007/s10008-020-04661-8.

Palomäki, T., Peltola, E., Sainio, S., Wester, N., Pitkänen, O., Kordas, K., Koskinen, J., and Laurila, T. (2018). Unmodified and multi-walled carbon nanotube modified tetrahedral amorphous carbon (ta-C) films as in vivo sensor materials for sensitive and selective detection of dopamine. Biosens. Bioelectron. *118*, 23–30. https://doi.org/10.1016/j.bios.2018.07.018.

Pan, J., Thierry, D., and Leygraf, C. (1996). Electrochemical impedance spectroscopy study of the passive oxide film on titanium for implant application. Electrochim. Acta *41*, 1143–1153. https://doi.org/10.1016/0013-4686(95)00465-3.

Pan, K., Fan, Y., Leng, T., Li, J., Xin, Z., Zhang, J., Hao, L., Gallop, J., Novoselov, K.S., and Hu, Z. (2018). Sustainable production of highly conductive multilayer graphene ink for wireless connectivity and IoT applications. Nat. Commun. *9*, 1–10. https://doi.org/10.1038/s41467-018-07632-w.

Park, S., and Ruoff, R.S. (2009). Chemical methods for the production of graphenes. Nat. Nanotechnol. *4*, 217–224. https://doi.org/10.1038/nnano.2009.58.

Patel, P.R., Popov, P., Caldwell, C.M., Welle, E.J., Egert, D., Pettibone, J.R., Roossien, D.H., Becker, J.B., Berke, J.D., Chestek, C.A., and Cai, D. (2020). High density carbon fiber arrays for chronic electrophysiology, fast scan cyclic voltammetry, and correlative anatomy. J. Neural. Eng. *17*, 056029. https://doi.org/10.1088/1741-2552/abb1f6.

Pham, V.H., Cuong, T.V., Hur, S.H., Shin, E.W., Kim, J.S., Chung, J.S., and Kim, E.J. (2010). Fast

and simple fabrication of a large transparent chemically-converted graphene film by spray-coating. Carbon *48*, 1945–1951. https://doi.org/10.1016/j.carbon.2010.01.062.

Piela, B., and Wrona, P.K. (1995). Capacitance of the gold electrode in 0.5 M H2SO4 solution: a.c. impedance studies. J. Electroanal. Chem. *388*, 69–79. https://doi.org/10.1016/0022-0728(94)03848-W.

Puthongkham, P., and Venton, B.J. (2019). Nanodiamond coating improves the sensitivity and antifouling properties of carbon fiber microelectrodes. ACS Sens. *4*, 2403–2411. https://doi.org/10.1021/acssensors.9b00994.

Robinson, J.T., Perkins, F.K., Snow, E.S., Wei, Z., and Sheehan, P.E. (2008). Reduced graphene oxide molecular sensors. Nano Lett. *8*, 3137–3140. https://doi.org/10.1021/nl8013007.

Roychaudhuri, C. (2015). A review on porous silicon based electrochemical biosensors: beyond surface area enhancement factor. Sens. Actuators, B *210*, 310–323. https://doi.org/10.1016/j.snb.2014.12.089.

Scalia, M., Sperini, M., and Guidi, F. (2012). The Johnson noise in biological matter. Math. Probl Eng. 582126. https://doi.org/10.1155/2012/582126.

Shao, Y., Wang, J., Engelhard, M., Wang, C., and Lin, Y. (2010). Facile and controllable electrochemical reduction of graphene oxide and its applications. J. Mater. Chem. *20*, 743–748. https://doi.org/10.1039/b917975e.

Shoval, A., Adams, C., David-Pur, M., Shein, M., Hanein, Y., and Sernagor, E. (2009). Carbon nanotube electrodes for effective interfacing with retinal tissue. Front. Neuroeng. *2*, 4. https://doi.org/10.3389/neuro.16.004.2009.

Sriprachuabwong, C., Karuwan, C., Wisitsorrat, A., Phokharatkul, D., Lomas, T., Sritongkham, P., and Tuantranont, A. (2012). Inkjet-printed graphene-PEDOT:PSS modified screen printed carbon electrode for biochemical sensing. J. Mater. Chem. *22*, 5478. https://doi.org/10.1039/c2jm14005e.

Stankovich, S., Dikin, D.A., Piner, R.D., Kohlhaas, K.A., Kleinhammes, A., Jia, Y., Wu, Y., Nguyen, S.T., and Ruoff, R.S. (2007). Synthesis of graphene-based nanosheets via chemical reduction of exfoliated graphite oxide. Carbon *45*, 1558–1565. https://doi.org/10.1016/j.carbon.2007.02.034.

Stepien, L., Roch, A., Tkachov, R., Leupolt, B., Han, L., van Ngo, N., and Leyens, C. (2017). Thermal operating window for PEDOT:PSS films and its related thermoelectric properties. Synth. Met. *225*, 49–54. https://doi.org/10.1016/j.synthmet.2016.11.017.

Thamilselvan, A., Manivel, P., Rajagopal, V., Nesakumar, N., and Suryanarayanan, V. (2019). Improved electrocatalytic activity of Au@Fe 3 O 4 magnetic nanoparticles for sensitive dopamine detection. Colloids Surf. B Biointerfaces *180*, 1–8. https://doi.org/10.1016/j.colsurfb.2019.04.034.

Turcheniuk, K., and Mochalin, V.N. (2017). Biomedical applications of nanodiamond (Review). Nanotechnology *28*, 252001. https://doi.org/10.1088/1361-6528/aa6ae4.

Venton, B.J., and Cao, Q. (2020). Fundamentals of fast-scan cyclic voltammetry for dopamine detection. Analyst *145*, 1158–1168. https://doi.org/10.1039/c9an01586h.

Vilarchao, M.E., Estebanez, L., Shulz, D.E., and Férézou, I. (2018). Supra-barrel distribution of directional tuning for global motion in the mouse somatosensory cortex. Cell Rep. *22*, 3534–3547. https://doi.org/10.1016/j.celrep.2018.03.006.

Li, D., Müller, M.B., Gilje, S., Kaner, R.B., and Wallace, G.G. (2008). Processable aqueous dispersions of graphene nanosheets. Nat. Nanotechnol. *3*, 101–105. https://doi.org/10.1038/nnano.2007.451.

Wang, Y., Li, Y., Tang, L., Lu, J., and Li, J. (2009). Application of graphene-modified electrode for selective detection of dopamine. Electrochem. Commun. *11*, 889–892. https://doi.org/10.1016/j.elecom.2009.02.013.

Wang, C., Du, J., Wang, H., Zou, C., Jiang, F., Yang, P., and Du, Y. (2014). A facile electrochemical sensor based on reduced graphene oxide and Au nanoplates modified glassy carbon electrode for simultaneous detection of ascorbic acid, dopamine and uric acid. Sens. Actuators B. *204*, 302–309. https://doi.org/10.1016/j.snb.2014.07.077.

Wang, J., Law, C.L., Mujumdar, A.S., and Xiao, H.W. (2017). The degradation mechanism and kinetics of Vitamin C in fruits and vegetables during thermal processing. In AS Fundamentals & applications (Part III — Drying Technologies for Foods: Fundamentals and Applications), P. Nema, B. Kaur, and Mujumdar., eds., pp. 227–253. Available at: https://www.researchgate.net/publication/319527724_The_Degradation_Mechanism_and_Kinetics_of_Vitamin_C_in_Fruits_and_Vegetables_During_Thermal_Processing.

Wang, Y., Chen, Y., Lacey, S.D., Xu, L., Xie, H., Li, T., Danner, V.A., and Hu, L. (2018). Reduced graphene oxide film with record-high conductivity and mobility. Mater. Today *21*, 186–192. https://doi.org/10.1016/j.mattod.2017.10.008.

Wang, K., Frewin, C.L., Esrafilzadeh, D., Yu, C., Wang, C., Pancrazio, J.J., Romero-Ortega, M., Jalili, R., and Wallace, G. (2019). High-performance graphene-fiber-based neural recording microelectrodes. Adv. Mater. *31*, 1805867. https://doi.org/10.1002/adma.201805867.

Weiland, J.D., and Humayun, M.S. (2014). Retinal prosthesis. IEEE Trans. Biomed. Eng. *61*, 1412–1424. https://doi.org/10.1109/TBME.2014.2314733.

Xu, Z., Ao, Z., Chu, D., Younis, A., Li, C.M., and Li, S. (2014). Reversible hydrophobic to hydrophilic transition in graphene via water splitting induced by UV irradiation. Sci. Rep. *4*. https://doi.org/10.1038/srep06450.

Yamagiwa, S., Fujishiro, A., Sawahata, H., Numano, R., Ishida, M., and Kawano, T. (2015). Layer-by-layer assembled nanorough iridium-oxide/platinum-black for low-voltage microscale electrode neurostimulation. Sens. Actuators, B *206*, 205–211. https://doi.org/10.1016/j.snb.2014.09.048.

Yang, J., and Gunasekaran, S. (2013). Electrochemically reduced graphene oxide sheets for use in high performance supercapacitors. Carbon *51*, 36–44. https://doi.org/10.1016/j.carbon.2012.08.003.

Yang, L., Liu, D., Huang, J., and You, T. (2014). Simultaneous determination of dopamine , ascorbic acid and uric acid at electrochemically reduced graphene oxide modified electrode. Sens. Actuators, B *193*, 166–172. https://doi.org/10.1016/j.snb.2013.11.104.

Yokota, R., Yamamoto, S., Yano, S., Sawaguchi, T., Hasegawa, M., Yamaguchi, H., Ozawa, H., and Sato, R. (2001). Molecular design of heat resistant polyimides having excellent processability and high glass transition temperature. High Perform. Polym. *13*, S61–S72. https://doi.org/10.1088/0954-0083/13/2/306.

Zhang, J., Yang, H., Shen, G., Cheng, P., Zhang, J., and Guo, S. (2010). Reduction of graphene oxide via l-ascorbic acid. Chem. Commun. *46*, 1112–1114. https://doi.org/10.1039/b917705a.

Zhang, L., Feng, J., Chou, K.C., Su, L., and Hou, X. (2017). Simultaneously electrochemical detection of uric acid and ascorbic acid using glassy carbon electrode modified with chrysanthemum-like titanium nitride. J. Electroanal. Chem. *803*, 11–18. https://doi.org/10.1016/j.jelechem.2017.09.006.

Zhu, J.J., and Connors, B.W. (1999). Intrinsic firing patterns and whisker-evoked synaptic responses of neurons in the rat barrel cortex. J. Neurophysiol. *81*, 1171–1183. https://doi.org/10.1152/jn.1999.81.3.1171.

Zhao, S., Liu, X., Xu, Z., Ren, H., Deng, B., Tang, M., Lu, L., Fu, X., Peng, H., Liu, Z., and Duan, X. (2016). Graphene encapsulated copper microwires as highly MRI compatible neural electrodes. Nano Lett. *16*, 7731–7738. https://doi.org/10.1021/acs.nanolett.6b03829.

STAR★METHODS

KEY RESOURCES TABLE

REAGENT or RESOURCE	SOURCE	IDENTIFIER
Chemicals, peptides, and recombinant proteins		
Highly Concentrated Graphene Oxide (HCGO, GO)	Graphene Supermarket	SKU: SKU-HCGO-W-60ML
L-ascorbic acid (Vitamin C, VC)	Millipore Sigma; Sigma Aldrich	CAS: 50-81-7 Product No.: A4403
1X Phosphate Buffered Saline Solution, pH 7.4 (1X PBS, PBS)	Quality Biological Inc.	Item No.: 114-058-101 UNSPSC: 12161700
Dopamine hydrochloride (Dopamine, DA)	Millipore Sigma; Sigma Aldrich	CAS: 62-31-7 Product No.: H8502
Potassium ferricyanide(iii) (Ferricyanide, $Fe(CN_6$, ferrocyanide, Red prussiate)	Millipore Sigma; Sigma Aldrich	CAS: 13746-66-2 Product No.: 702587
Experimental models: organisms/strains		
Rat: Adult Male Sprague Dawley, Crl:CD(SD), 225g	Charles River Laboratories	RGD ID: 734476 Ontology ID: RS:0000064 University of Pennsylvania IACUC Protocol No. 806241
Software and algorithms		
MATLAB	MATLAB	Custom scripts were created to handle plotting and presentation of the data collected.

RESOURCE AVAILABILITY

Lead contact

For further information or requests for resources, reagents, and other matters, please connect with the lead contact and corresponding author, Dr. Flavia Vitale (vitalef@pennmedicine.upenn.edu).

Materials availability

This study did not generate any new or unique reagents. All materials used in this study (including reagents and animals) are commercially available, and details for purchasing them may be found in the Key resources table (KRT).

Data and code availability

- All data reported in this paper will be shared by the lead contact and corresponding author upon request.
- This paper does not report original code.
- Any additional information required to reanalyze the data reported in this paper is available from the lead contact upon request.

EXPERIMENTAL MODEL AND SUBJECT DETAILS

For in vivo animal studies, one male rat (Crl:SD, 225 g) was used for an acute neural recording session with the rGO/Au μECoG array. Anesthesia was induced with 5% isoflurane in oxygen. The anesthetized rat was placed in a stereotaxic frame with his body resting on a heating pad. Buprenorphine SR was administered for systemic analgesia. A midline scalp incision site was shaved, cleaned, and injected with line block of 0.25% bupivacaine. Respiratory rate and pedal and palpebral reflexes were checked every 10 min to verify depth of anesthesia, which was maintained with 3–3.5% isoflurane. The scalp was incised to expose the dorsal skull and a craniotomy of the right parietal bone was performed to expose the vibrissal representations of primary somatosensory cortex (*i.e.*, barrel cortex). Two 00–90 skull screws with attached gold pins were implanted: one in the left frontal bone (recording ground) and one in the left occipital bone (recording

reference). The rGO/Au μECoG array was glued to the bottom of a custom designed 3D-printed rod that was mounted in a stereotaxic microdrive. The microdrive was angled 30° from vertical, and the array was lowered to press gently into the pial surface of the barrel cortex. Individual contralateral whiskers were deflected using a custom stimulation system. The whiskers were cut to a length of approximately 1 cm and inserted at their natural angle into a glass capillary tube (0.23 mm inner diameter) that was epoxied to a piezoelectric bender (Thorlabs, Inc.). Each deflection consisted of a pulse with 2 ms rise time, 2 ms plateau, and 2 ms fall time that was smoothed to prevent mechanical ringing. These whisker stimuli were delivered at 0.5 Hz while wideband neural signals were recorded at 20 kHz per channel using an Intan RHS system (Intan Technologies). To distinguish evoked neural activity from any noise introduced by the stimulation system, whisker stimulation recordings were interleaved with control recordings, in which the same stimuli were delivered but with the whisker removed from the capillary tube. All animal procedures were approved by the Institutional Animal Care and Use Committee of the University of Pennsylvania (IACUC Protocol No. 806241).

METHOD DETAILS

Preparation of GO + VC solutions

Highly concentrated GO (>5 mg mL^{-1}) was purchased from Graphene Supermarket® and was used for all experiments. VC in powder form was purchased from Sigma Aldrich, and VC solutions were made at the appropriate concentrations by dissolving powder in deionized water over 30 min under continuous magnetic stirring at room temperature. All GO + VC mixtures were made by combining GO and VC solutions in a 1:1 volume ratio and vortex mixing for 5 min.

Spray-coating techniques

Prior to spray-coating, the surface of the target substrate was activated with an air plasma (Harrick PDC-32G Basic Plasma Cleaner, p_{base} = 305 mTorr, plasma power = 18 W, exposure time = 2 min). The substrates used in this report included precleaned microscope slides (Fisherbrand 12-550-A3, 25x75x1 mm), cut into 25 mm × 25 mm squares, and 3″ diameter Si wafers coated with parylene-C and prepatterned with Au contacts. After plasma activation, samples were placed on a hot plate at 150°C and preheated for 5 min. (Figure 1A). Subsequently, 3 mL of the GO + VC solutions were spray-cast onto the sample using a commercial airbrush (Gocheer) connected to a TC-20 air compressor unit (Figure 1B). The average spraying pressure was ~0.25 MPa (36 psi), and the average distance between the airbrush and substrate was 12–15 cm. Following spray-coating of the GO + VC solutions, samples were left on the hot plate at 150°C in order to complete the reduction step and produce VC-rGO films (Figure 1C). To optimize the reduction process, VC concentration and film heating time at 150°C were varied between 1 and 50 mM and 2.5–30 min, respectively.

Film characterization

Sheet resistance: R_s, of VC-rGO films was measured with a Loresta-AX MCP-T370 handheld low resistivity four-point probe (Nittoseiko Analytech Co., Ltd.). Profilometry was performed with a Tencor KLA P-7 Stylus Profiler (KLA Corp.; scan speed = 50 μm s^{-1}; sampling frequency, f_s = 200 Hz; stylus applied force, f_{appl} = 2 mg) to determine VC-rGO film thickness, τ. After measuring the values of sheet resistance and average thickness, the DC conductivity of the films, σ_{DC}, was calculated using the relationship $\sigma_{DC} = (Rs \cdot \tau)^{-1}$.

Raman: spectra were collected using an NT-MDT Ntegra Raman-NSOM system, with a 532 nm excitation laser. The effective wavelength range was limited to 180–2,580 cm^{-1}. Raman spectra were averaged across N = 6 separate scans, and then fitted with a Lorentzian function in MATLAB to determine peak positions and intensities for the peaks specific to graphitic carbon (*i.e.*, the D and G bands).

Imaging: a JSM-7500F scanning electron microscope (SEM; JEOL, Ltd.) with a 3 keV accelerating voltage was used for imaging VC-rGO thin films on glass substrates. A Bruker Icon atomic force microscope (AFM; Bruker Corp.) was used to characterize the flake morphology of GO + VC and VC-rGO thin films on glass substrates, and ImageJ was used to help identify individual flakes in the collected micrographs.

Monitoring the DC conductivity over 1 month

VC-rGO films were made with the optimized VC reduction method (50 mM VC, 15 min at 150°C), followed by aging in air at room temperature, or submerged in 1X PBS at room temperature. DC conductivity of the

films was measured at the initial (t_0) and final (30 days) timepoints using a 4-point probe (Figure S3). To quantify the total conductivity retained after aging, $\%\Delta\sigma_{DC}$, we defined the following parameter:

$$\%\Delta\sigma_{DC} \equiv \left(\frac{\sigma_f}{\sigma_0}\right) \times 100$$

where σ_0 is the DC conductivity at t_0, and σ_f is the DC conductivity at the final timepoint.

Fabrication of μECoG devices

rGO/Au μECoG arrays were fabricated following previously published methods (Driscoll et al., 2020; Murphy et al., 2020). Briefly, a Si wafer was coated with 4 μm of parylene-C and patterned with electrode traces consisting of 10nm/100nm Ti/Au using photolithography, electron-beam deposition, and lift-off. 1% Micro-90 cleaning solution was spin-cast onto the wafer as an anti-adhesion layer, and a 3 μm-thick sacrificial parylene-C layer was deposited. Openings over the Au traces were made in the sacrificial parylene layer via photolithography and reactive ion etching (RIE). Next, 3 mL of the GO + VC mixture was spray-cast onto the wafer. The sacrificial parylene layer was then manually removed, leaving behind GO + VC films only in the areas defined by the previous patterning steps. The GO + VC films were subsequently reduced by heating the entire wafer on a hot plate at 150°C for 15 min. After the reduction step, a top encapsulation layer of 4 μm of parylene-C was deposited, and device outlines were patterned via photolithography and lift-off techniques. A final RIE step removed residual parylene, and the rGO/Au microelectrodes were finally peeled off from the Si wafer for characterization and use. Plain Au electrodes were made using a similar fabrication flow, only excluding the sacrificial parylene patterning, GO + VC spray-coating, and reduction steps.

Characterization of μECoG devices *in vitro*

Completed μECoG arrays were imaged using a Keyence VHX-6000 Digital Light Microscope (Keyence Corp.). The devices were then loaded into zero-insertion force (ZIF) connectors soldered to custom Omnetics printed circuit boards (PCBs; DigiKey Electronics). A Gamry Reference 600 potentiostat/galvanostat/ZRA (Gamry Instruments, Inc.) was used for all electrochemical characterization *in vitro*. In particular, we conducted electrochemical impedance spectroscopy (EIS), cyclic voltammetry (CV), chronopotentiometry and continuous charge-injection tests to measure the electrochemical impedance, cathodal charge storage capacity (CSC_C), safe charge injection limit (Q_{inj}), total charge injection capacity (CIC), and long-term pulsing stability of the μECoG devices. All *in vitro* testing was conducted in 1X phosphate buffered saline (PBS; pH 7.4, Quality Biological) at room temperature, using a standard three-electrode cell featuring a graphite rod counter electrode (1-cm diameter; Bio-Rad Laboratories, Inc.), and an aqueous Ag/AgCl reference (3M KCl; Sigma Aldrich). Specifically, EIS was measured with a 10 mV_{rms} input voltage, sweeping the frequency from 1–10^5 Hz. Impedance spectra were subsequently fitted with equivalent circuit models in Gamry's *EChem Analyst* software (see Fitting procedure details below), to obtain values of charge-transfer resistance (R_{ct}) and double-layer capacitance (C_{dl}). CVs were completed first in Au's safe operating window (Ganji et al., 2017a; Ganji et al., 2017b), then in the rGO operating window, at a scan rate of 200 mV s^{-1}. The first scan was always completed in the cathodic direction (*i.e.*, towards the negative potential limit first). Values of Q_{inj} were determined from both CVs and impedance fitting results, using the equation (Cogan, 2008; Apollo et al., 2015),

$$Q_{inj} = \frac{C_{dl} \cdot V_{OW}}{GSA} \qquad \text{(Equation 1)}$$

where V_{OW} is the size of the electrode's full operating voltage window (also known as the electrochemical window or the water window), and GSA is the electrode geometric surface area. During chronopotentiometry experiments, voltage transients were recorded in response to biphasic current pulses of 7.5 μA amplitude and 650 μs duration, with the cathodic pulse delivered first and a 20-μs interpulse interval (Ganji et al., 2017b). In the continuous charge-injection tests, charge was injected through the electrodes at 500 μC cm^{-2} per phase (current amplitude, 1.56 μA $phase^{-1}$) at 130 Hz over 24 h (Dalrymple et al., 2019), and the electrode impedance was measured every 260,000 pulses. The starting open circuit potential (OCP) was 0 V for all measurements described above.

Fitting procedures for μECoG devices in 1X PBS

A modified Randles cell was used to fit the impedance spectra of the bare Au electrodes (Franks et al., 2005; Boehler et al., 2020). The coating model used to describe the rGO/Au electrodes describes coatings on

metallic or Si electrodes (Pan et al., 1996). For both models, we used a constant phase element (CPE) in place of the traditional double-layer capacitance, C_{dl}, in order to account for the non-ideal behavior of the interfacial double-layer (Kochowski and Nitsch, 2002).

C_{dl} values reported in the main manuscript and in Table S2 were calculated from CPE parameters using the equation (Hirschorn et al., 2010; Bera et al., 2017).

$$C_{dl} \equiv \frac{(Y_0 R_{sol})^{1/\alpha}}{R_{sol}},$$

where R_{sol} is the solution/spreading resistance with units of Ω, Y_0 is the CPE admittance with units of $S\ s^{\alpha}$, and α is the unitless CPE constant ($_{\alpha}$ = 1 represents a perfect capacitor, $_{\alpha}$ = 0 is a perfect resistor).

In addition to C_{dl}, it is also possible to calculate the theoretical value of the solution resistance, R_{sol}^{th}, using the equation (Franks et al., 2005)

$$R_{sol}^{th} \equiv \frac{\rho \ln 4}{\pi l},$$

where ρ is the solution resistivity (72 Ω cm for 1X PBS), and l is the electrode side-length (here, 50 μm). For the Au and rGO/Au electrodes in this work, R_{sol}^{th} = 6.354 kΩ, which is in excellent agreement with experimentally fitted values of R_{sol}, supporting the validity of our proposed models (Table S2).

Evaluating the total charge injection capacity

The total charge injection capacity (CIC) of a stimulating technology defines the maximum charge that an electrode can inject into a solution (or into tissue) such that all reactions that occur are entirely reversible. In terms of electrochemical parameters, the CIC can be defined as the total charge (current × time [pulse width]) at which the maximum excursion/polarization potential, E_m, exceeds the water window limits of the electrode material, either in the anodic or cathodic phase (Ganji et al., 2017b; Cisnal et al., 2018; Driscoll et al., 2021). To determine the CIC, then, the polarization potential, E_m, must first be defined. E_m is best summarized by the equation (Cisnal et al., 2018).

$$E_m = E_{p,i} + \Delta E_p = E_{p,i} + (\Delta V - V_a),$$

where $E_{p,i}$ is the initial offset voltage (typically 0 V), and ΔE_p is the polarization potential of the electrode across the electrode-electrolyte interface. ΔE_p can be determined from voltage transient experiments, as it is equivalent to the voltage transient response, ΔV, after subtracting the access voltage, V_a, which is the instantaneous potential change at the beginning of, or immediately after, current pulse delivery (Figure S6).

Dopamine and ferrocyanide detection *in vitro*

Dopamine and potassium ferrocyanide were purchased in powder form from Sigma Aldrich and test solutions were made by dissolving the powders in 1X PBS by vigorous hand shaking, followed by vortex mixing for 5 min. For DA sensing, CVs were completed from −0.4 V to +1.0 V at a scan rate of 4 V s^{-1} in a three electrode configuration, with a carbon rod counter electrode and aqueous Ag/AgCl reference. For detecting $Fe(CN)_6$, the same three-electrode configuration was used, but CVs were completed from 0.0 V to +0.6 V at a scan rate of 50 mV s^{-1}. In both instances, the first scan was always completed in the cathodic direction, the initial OCP was 0 V, and no nitrogen or argon bubbling was used before, during, or after the CVs were measured. Different rGO/Au μECoG arrays were used for DA detection and $Fe(CN)_6$ detection, and these arrays were also separate from those used for EIS measurements, so as to avoid any potential complications that might have been caused by DA adsorption.

Peak oxidation currents were determined using standard techniques after background subtraction (Elgrishi et al., 2018; Espinoza et al., 2019), and a calibration curve was constructed for DA in the 1–50 μM concentration range (Venton and Cao, 2020). The sensitivity of the rGO/Au electrodes for DA detection was calculated from the slope, m, of the fitting curve (in units of nA μM^{-1}), and the limit of detection (LOD) was calculated using the equation (Palomäki et al., 2018; Manbohi and Ahmadi, 2019),

$$LOD = \frac{3s_B}{m} \qquad \text{(Equation 2)}$$

where s_B is the standard deviation of the background current in amperes.

To estimate the effective electrochemical surface area of the rGO/Au μECoG electrodes, A_{ESA}, we applied the simplified Randles-Sevcik equation at room temperature to the $Fe(CN)_6$ data (Kang et al., 2012; Wang et al., 2014),

$$i_p = \left(2.69 \times 10^5\right) AC\sqrt{n^3 D\nu} \qquad \text{(Equation 3)}$$

where i_p is the background-subtracted peak current in amperes, A is the electrode area in cm^2, C is the concentration of the solution in mol cm^{-3}, n is the number of electrons transferred in the $Fe(CN)_6$ redox event, D is the diffusion coefficient of $Fe(CN)_6$ in $cm^2\ s^{-1}$, and $_v$ is the scan rate in V s^{-1}.

QUANTIFICATION AND STATISTICAL ANALYSIS

The average values cited in this work were defined as the sum of the relevant measurement terms, Σ(terms), divided by the total number of relevant measurement terms, N_{terms}:

$$\mu = \frac{\sum(\text{terms})}{N_{terms}}.$$

The standard deviations in this work were calculated as the square root of the variance, where the variance was defined as the sum of the squared differences between each relevant measurement term and the average value of that same measurement term, $\Sigma(terms_i\text{-}\mu)^2$, then divided by the total number of relevant measurement terms, N_{terms}:

$$\sigma = \sqrt{\sum \frac{(\text{terms}_i - \mu)^2}{N_{terms}}}.$$

The average values and standard deviations for each relevant measurement term are cited in the main manuscript, and are also provided in the Figures and Tables of the main manuscript and Supplemental information.

The only statistical tests applied in this study were Student's *t*-tests used to compare values of R_{ct} and C_{dl} between Au and rGO/Au μECoG fitting results. These analyses were run across n = 4 separate electrodes, with significance defined as a p-value $p < 0.05$. Statistical results are cited in the main manuscript, and can also be found in Figure S4.